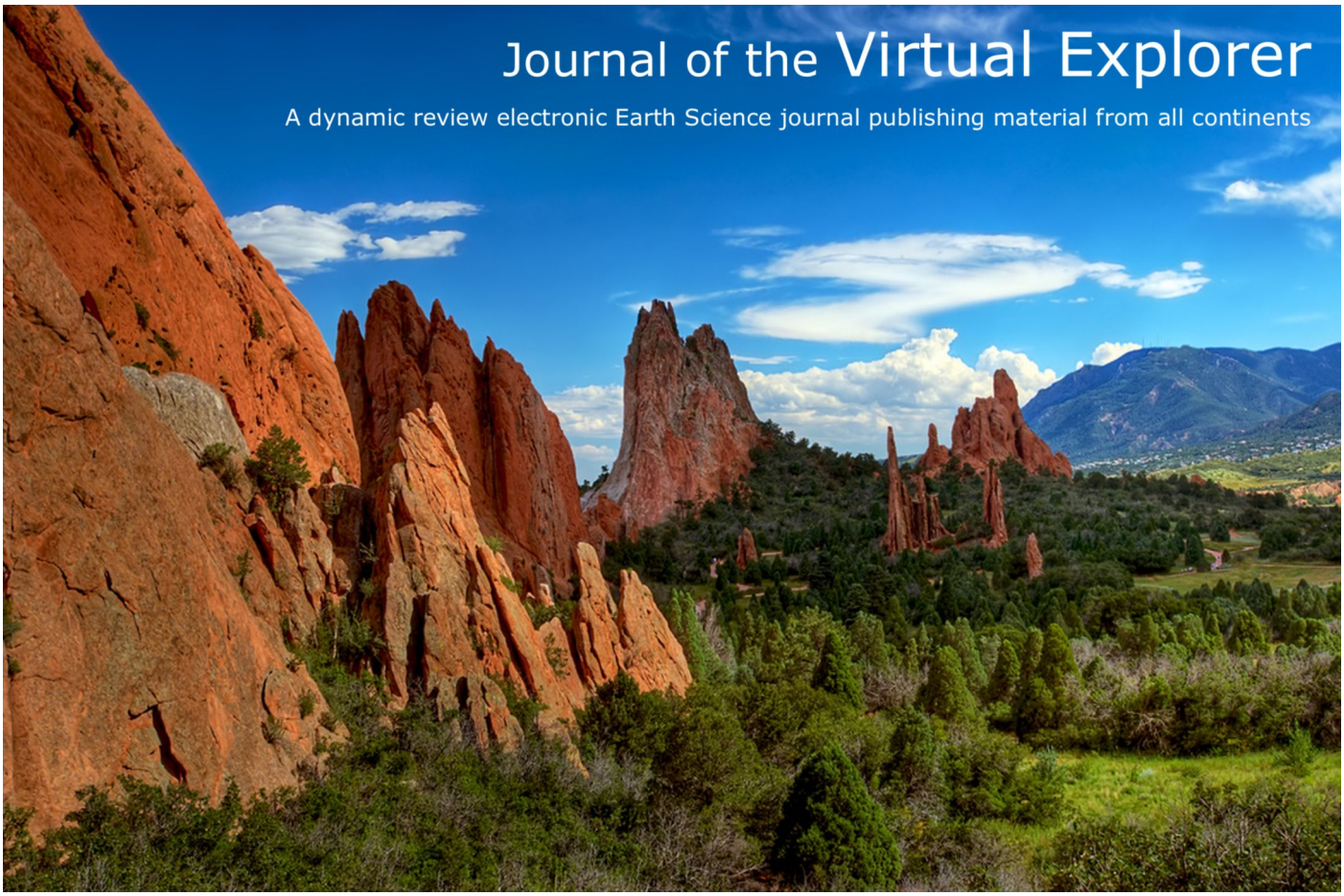

Coronitic microstructures in patchy eclogitised continental crust: the Lago della Vecchia pre-Alpine metagranite (Sesia-Lanzo Zone, Western Italian Alps)

Michele Zucali

Journal of the Virtual Explorer, Electronic Edition, ISSN 1441-8142, volume **38**, paper 5
In: (Eds.) M.A. Forster and J.D. Fitz Gerald, The Science of Microstructure - Part II, 2011.

Download from: http://virtualexplorer.com.au/article/2011/286/lago-della-vecchia-permian-metagranite

Click http://virtualexplorer.com.au/subscribe/ to subscribe to the Journal of the Virtual Explorer.
Email team@virtualexplorer.com.au to contact a member of the Virtual Explorer team.

Journal of the Virtual Explorer, 2011
Volume 38
Paper 5
http://virtualexplorer.com.au/

Coronitic microstructures in patchy eclogitised continental crust: the Lago della Vecchia pre-Alpine metagranite (Sesia-Lanzo Zone, Western Italian Alps)

Michele Zucali
Dipartimento di Scienze della Terra "A. Desio" - Università degli Studi di Milano, Via Mangiagalli, 34 - 20133 Milano, Italy. *Email: michele.zucali@unimi.it*

Abstract: The *Lago della Vecchia* pre-Alpine coronitic metagranite (Sesia-Lanzo Zone, Western Italian Alps, Valle del Cervo) preserves igneous textures and mineralogy despite the complete eclogitization recorded by surrounding deformed metagranites and country rocks. The coronitic cores are metre to few metres undeformed metagranites preserving igneous cm-sized K-feldspar and mm-sized biotite. Microscale analysis shows that igneous association is partly preserved: biotite, white mica and K-feldspar are only partly replaced by Alpine assemblages, while the original plagioclase is pseudomorphically overgrown by aggregates of albite + phengitic mica + Fe-epidote ± garnet. Metamorphic reactions are also localized at the interfaces biotite – plagioclase and white mica – plagioclase. A continuous garnet corona with a distinctive partitioning of Ca^{2+} and Fe^{2+} occurs between biotite and plagioclase, suggesting diffusive mass transfer during a prograde burial path.

Microdomains have been described and analysed in terms of their geometry, mineral composition and chemistry patterns using optical microscopy, X-rays compositional maps, chemical analyses and image analysis in order to detail the microstructures and to reconstruct the relative chronology of the reactions within each microdomain.

The results allow demonstration of the chemical exchanges that occurred between adjacent igneous microdomains:

- Biotite microdomain at contact with plagioclase – two coronas are observed: 1) Bt_{II} + Phn-Wm_{II} + Alm-rich Grt_I; 2) Phn-Wm_{II} + Grs-rich Grt coronas;
- White mica microdomain with plagioclase: a single Phn-Wm_{II} + Grt + Ep + Ab corona develops;
- K-feldspar microdomain with plagioclase: a single Ab + Phn-Wm_{II} ± Ep ± Grt corona develops;
- Plagioclase core microdomain: Ab + Phn-Wm_{II} (fine-grained) + Ep ± Grt;
- K-feldspar core microdomain: large igneous grains are partly to completely replaced by Ab from the plagioclase-K-feldspar boundaries or along fractures.

The absence of deformation seems to inhibit the complete development of eclogite-facies metamorphic parageneses, allowing the preservation of microstructures, mineral phases and chemistry. This information is commonly hidden by the widespread development of high pressure - low temperature eclogite-facies assemblages within surrounded deformed volumes.

Citation: 2011. Coronitic microstructures in patchy eclogitised continental crust: the Lago della Vecchia pre-Alpine metagranite (Sesia-Lanzo Zone, Western Italian Alps). In: (Eds.) M.A. Forster and J.D. Fitz Gerald, *Journal of the Virtual Explorer*, volume **38**, paper 5, doi: 10.3809/jvirtex.2011.00286

Introduction

Coronitic rock volumes preserve the structural and chemical memory of geological events that are commonly not preserved in intermediate to high strain rock volumes (Lardeaux and Spalla, 1991; Spalla *et al.* 2004; Holyoke and Tullis, 2006). The new metamorphic phases generally grow by developing corona textures rather than new planar fabrics, allowing the preservation of the composition of old microdomains. These features allow to relate reaction products to their reactants and investigate the relative timing of reactions with respect to the chemical and mechanical changes in individual microdomains as well in the surrounding rocks.

Corona textures may allow the identification of metamorphic reactions (Vernon and Clarke, 2008) and subsequently, when thermobarometry and geochronology is undertaken, the reconstruction of the *P-T-t* paths.

In this contribution a microstructural analysis of a pre-Alpine (Permian?) metagranite is presented; the patchy distribution of high pressure – low temperature metamorphism allowed partial preservation of the microstructures and chemical compositions of the primary igneous phases, along with preservation of prograde to retrograde assemblages.

The geometry, mineral composition and chemistry patterns of igneous microdomains are investigated using optical microscopy, X-rays compositional maps, chemical analyses and overall image analysis, in order to detail the microstructural evolution and to reconstruct the relative chronology of the reactions.

Geological Setting

The Sesia-Lanzo Zone (SLZ) belongs to the Austroalpine Domain of the Western Alps (Fig. 1) and is interpreted as a slice of the Adria convergent continental margin (e.g. Polino *et al.* 1990) that recorded a pervasive Alpine HP metamorphism (Compagnoni *et al.* 1977). The SLZ is now bounded by relicts of the Ligurian-Piemontese Tethys to the north and by the Insubric-Tonale line (Canavese line) to the south; the latter divides the SLZ from the Southern Alpine Ivrea Zone (Fig. 1). During Alpine subduction, the SLZ was tectonically eroded from the upper continental margin (Polino *et al.* 1990) and subducted to depths > 60 km. During the Cretaceous, the SLZ records a pervasive eclogite-facies re-equilibration. During the Cretaceous, the SLZ records a pervasive eclogite-facies re-equilibration.

Afterwards, it was partially affected by a greenschist-facies event, associated with the exhumation to the uppermost part of the Tertiary nappe stack (Passchier *et al.* 1981; Inger *et al.* 1996; Duchene *et al.* 1997; Rubatto *et al.* 1999; Zucali *et al.* 2002b; Zucali and Spalla, 2011).

On the basis of its lithological composition and dominant metamorphic imprint, the SLZ has been subdivided into two tectonic units (Fig. 1): the upper unit, the II Dioritic Kinzigitic Zone, shows a dominant metamorphic imprint under amphibolite to granulite facies conditions of pre-Alpine age. The lower unit, which consists of metapelites, metabasics and metagranitoids locally preserving Permian igneous bodies (e.g. Monte Mucrone and Val Sermenza gabbro), is divided into three complexes that record a pervasive Alpine metamorphic imprint: the Gneiss Minuti Complex (GMC) that preserves a dominant metamorphic imprint under greenschist facies conditions, the Eclogitic Micaschist Complex (EMC) that preserves dominant metamorphic imprint under eclogite facies conditions and the Rocca Canavese Thrust Sheet (Pognante 1989b; Spalla and Zulbati 2004) where a lawsonite blueschists-facies metamorphic imprint characterizes the peak stage. The eclogitic imprint has been dated to Late Cretaceous-Early Palaeocene (Oberhänsli *et al.* 1985; Inger *et al.* 1996; Duchene *et al.* 1997; Ruffet *et al.* 1997; Rubatto *et al.* 1999; Handy *et al.* 2005; Babist *et al.* 2006; Konrad-Schmolke *et al.* 2006). The area of study is located in the EMC.

Within portions of the SLZ during its pre-Alpine evolution a penetrative amphibolite foliation was imprinted in metapelites and in basic granulites, overprinting granulite facies assemblages (Lardeaux and Spalla 1991). *P-T* estimates for this pre-Alpine evolution indicate an early metamorphic imprint at $0.6 \leq P \leq 0.9$ GPa and T = 700 - 900°C, followed by a re-equilibration stage at P = 0.3 - 0.5 GPa and T = 570 - 670 °C. A greenschist-facies retrogression is recorded at P = 0.25 - 0.35 and T < 550°C (Lardeaux and Spalla 1991). Similar *P-T* conditions have been estimated for the crystallization of Permian intrusives (Zucali *et al.*, 2002b).

In the Monte Mucrone-Mars area and around Alpe Toso, Val Sesia, pre-Alpine mineralogical and textural remnants are preserved, where amphibolite-facies pre-Alpine paraschists and metabasics are intruded by granitoids of Permian age (Oberhänsli *et al.* 1985; Paquette *et al.* 1989). In the Southern SLZ, acidic and mafic pre-Alpine granulites are well preserved and associated with

granulitised gabbros, characterized by a similar pre-Alpine *P-T* evolutions (Rebay and Spalla 2001).

Alpine *P-T* conditions for the eclogitic stage have been estimated at $P > 1.5$ GPa and $T = 500 - 600$ °C (Desmons and O'Neil 1978; Koons 1986; Tropper *et al.* 1999; Zucali *et al.* 2002a, 2004, 2011). Prograde and retrograde *P-T* conditions are characterized by lawsonite-bearing assemblages in some localities, implying a low geothermal regime active during both prograde and retrograde evolution (Pognante 1989a, 1989b; Matsumoto and Hirajima 2004; Zucali *et al.* 2004; Zucali and Spalla, 2011).

The innermost part of Sesia-Lanzo Zone (EMC) was intruded by the Biella Oligocene Pluton between 29-31 Ma (Bigioggero *et al.* 1994; Romer *et al.* 1996; Zanoni *et al.* 2008) while the andesitic dykes, that crosscut all Alpine fabrics, have ages between 29 and 33 Ma (Scheuring *et al.* 1973; Kapferer *et al.* 2011).

The *Lago della Vecchia* area (Piemonte, Italy, UTM coordinates: 1413689.522 - 5058432.551;1413689.522 - 5058432.551) belongs to the SLZ and it is mainly constituted by variably deformed metagranitoids characterized by a eclogite facies metamorphic overprint.

Figure 1. The Sesia-Lanzo Zone

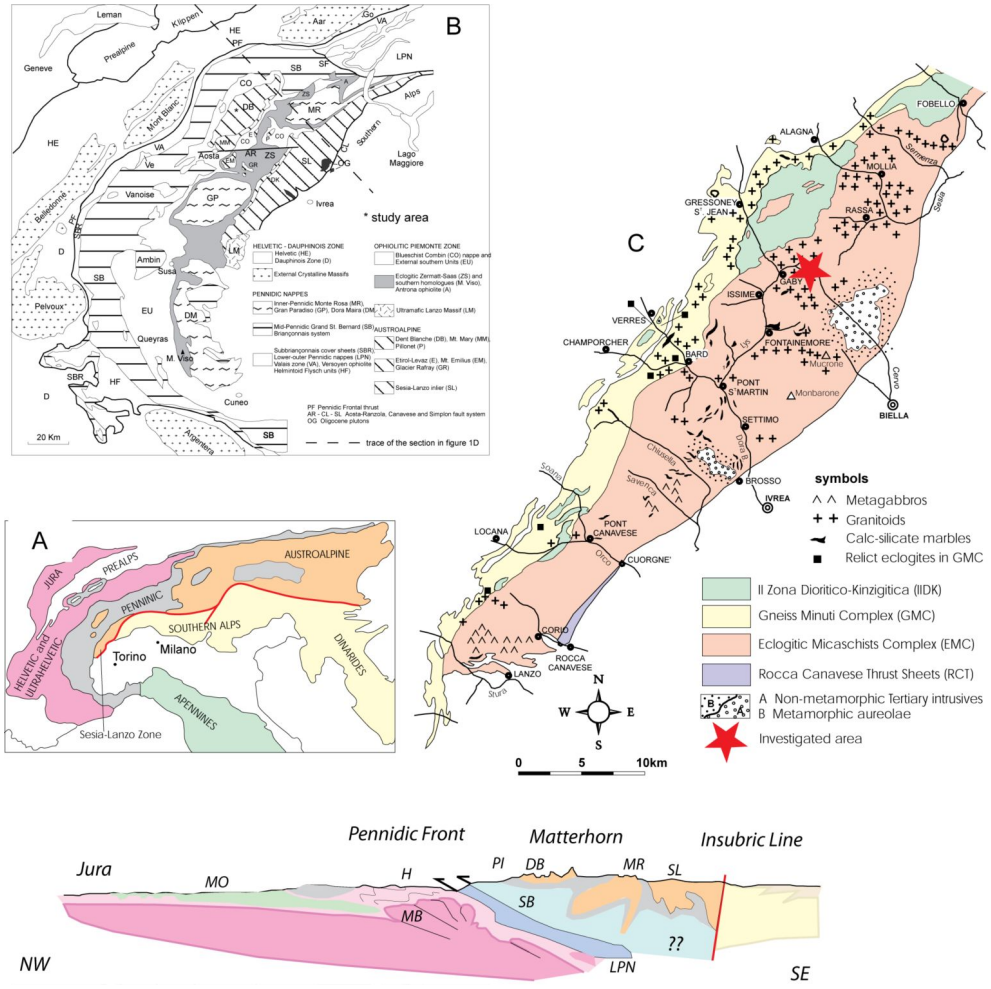

A) Tectonic outline of the Alpine chain. B) Geological outline of Western Alps (redrawn after Dal Piaz *et al.* 2001). C) Classical subdivision of the Sesia-Lanzo Zone. The red star indicates the investigated area. D) NW-SE geological cross-section along the Western Alps: SA= Southern Alps; SL= Sesia-Lanzo Zone; MR = Monte Rosa; DB= Dent-Blanche; PI= Penninic; SB= Grand Saint Bernard; MB= Mont Blanc; LPN= Lower Penninic; H= Helvetic; MO= Molasse.

Lithotypes and mesostructures

The area is characterized by a penetrative mineralogical foliation marked by SPO of eclogite facies minerals, varying as a function of the bulk rock chemistry. Lithotype distribution and mesostructures are reported in Figure 2. Mineral abbreviations after Kretz (1983).

Figure 2. Simplified geological-structural map of the *Lago della Vecchia* area. Original field survey at scale 1:5.000.

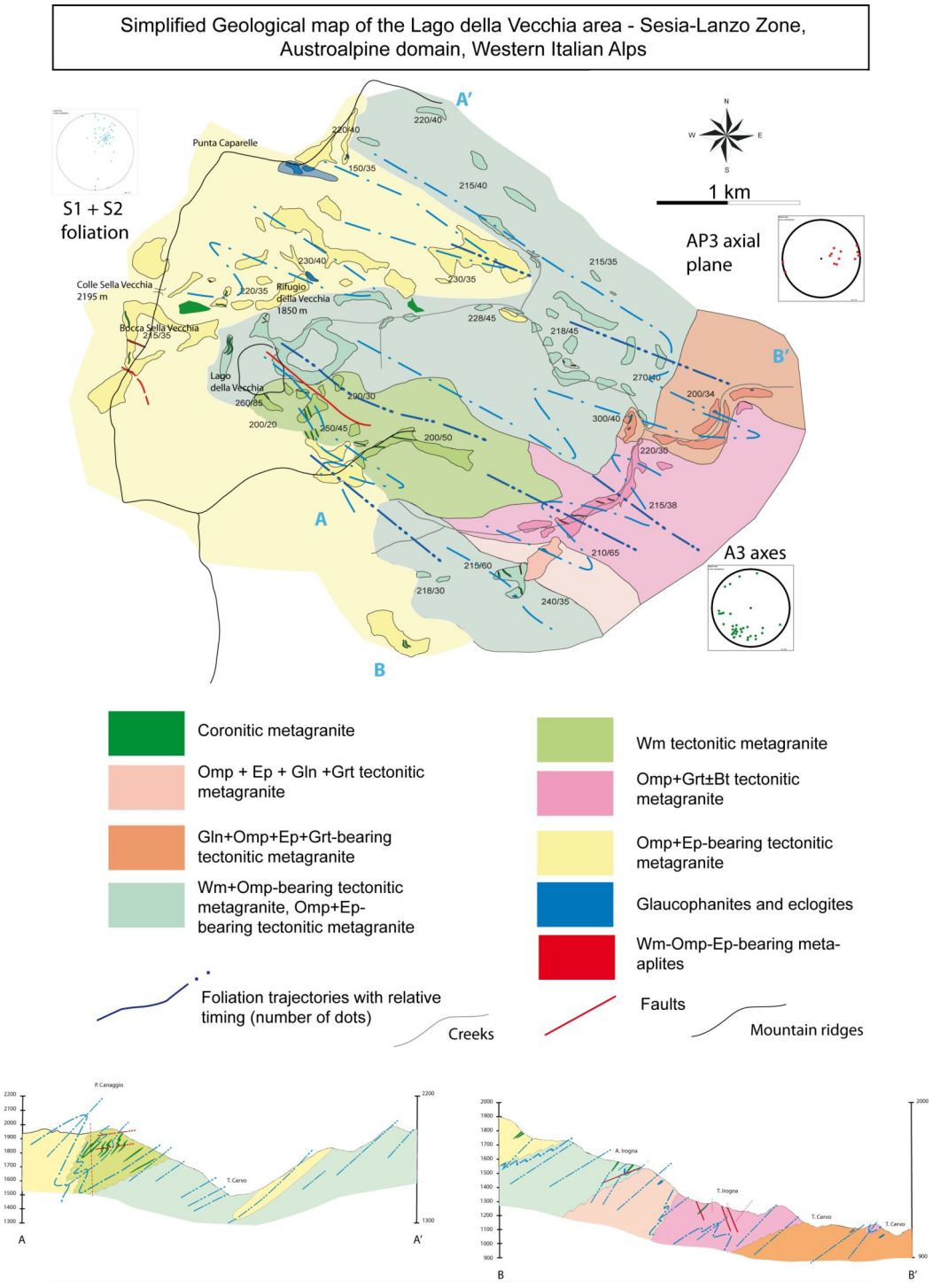

Mineral abbreviations after Kretz (1983).

Lithotypes

Metagranites are divided into two groups, distinguished on the basis of mesoscopic fabrics: 1) Coronitic metagranites and 2) deformed metagranites; minor lithotypes are metapelites, glaucophanites, eclogites and dykes, further distinguished on the basis of their mineral assemblages.

The deformed metagranites constitute the most common lithotype in the area (Fig. 2); they are characterized by a well-developed foliation marked by shape preferred orientation (SPO) of white mica and quartz (Fig. 2). Omphacite and glaucophane are also characterized by SPO generally parallel to the main foliation. Eclogites occur as decametre to metre-thick boudins within deformed metagranites (Fig. 2). Glaucophanite bodies may reach ten of meters of width and hundred of meters of length. The SPO of glaucophane marks the lineation within glaucophanites whereas the SPO of omphacite defines the lineation in eclogites.

Coronitic (i.e. undeformed) metagranites have been found in two localities within phengitic-mica + omphacite-bearing gneisses as meter-size lenses (Fig. 2). Coronitic metagranite is constitute by quartz (30-40%) + plagioclase (30-35%) + biotite (15-25%) + K-feldspar (5-10%) ± white mica (< 5%). K-feldspar, biotite and plagioclase are euhedral to subhedral while quartz is anhedral being interstitial among other phases. The aggregates of coronitic metagranites are inequigranular, polygonal to interlobate where K-feldspar defines up to 1.5 cm crystals (Fig. 3a); plagioclase, biotite, white mica and quartz size varies from < 2 mm to 5 mm.

Geological evolution and mesostructures

Geological map of figure 2 shows the distribution of main structures; the area is characterized by a penetrative mineralogical foliation marked by SPO of eclogite facies minerals, varying as a function of the bulk rock chemistry.

As metre-scale relict volumes, undeformed igneous textures are still preserved, wrapped by the eclogitic foliations. Magmatic structures are abbreviated Mag while deformational D, both with subscripts that refers to the relative chronology, from older (e.g. Mag0) to younger (D5).

On the basis of the mesostructural overprinting relations the following superimposed groups of structures have been divided:

Isotropic textures are preserved in coronitic metagranites (Mag0) (Fig. 3a). They are characterized by preserved biotite, K-feldspar and plagioclase euhedral-subhedral grains and interstitial quartz. Biotite preserves a dark red color and its size ranges from 0.5 cm to 2 cm. K-feldspar may occur as white to pink up to 2.5 cm grains. Plagioclase has a white to greenish colour and sizes from 1 to 2 cm.

During D1 and D2 a mm-thick foliation develops within deformed metagranites (S1); S1 is marked by SPO of white-mica, quartz and omphacite; cm-thick omphacite grains also define S1 (Fig. 3b,c,d). Glaucophane SPO marks the S1 foliation within glaucophane-bearing deformed metagranitoids together with Wm aggregates. During D1 boudinage occurs, producing meter-scale boudins of eclogites and glaucophanites. Within boudins the S1 foliation is marked by SPO of omphacite, glaucophane and white mica.

During D2, S1 is folded (Fig. 3c) and an axial planar foliation S2 formed. S2 is marked by the SPO of white mica, omphacite, glaucophane and quartz in deformed metagranites; elongated boudins of eclogites and glaucophanites also occur parallel to S2 (Fig. 3e,g). Within the boudins S1 shows an high angle with respect to external S2 and lithological boundaries.

D3 is associated with open folding at metre-scale with steep axial plane E-W dipping. D3 folding is generally associated with discrete ductile-brittle shear zones and a localised crenulation cleavage marked by white mica ± chlorite.

During Mag4 the intrusion of andesitic dykes occurs in the whole area. Andesitic dykes are 50cm to 1-2m thick and generally crosscut all lithotypes and foliations. These dykes have been dated across the Sesia-Lanzo Zone at about 29-33 Ma (Scheuring *et al.* 1973; Kapferer *et al.* 2009) (Fig. 3h).

D5 is associated with fracturing and faulting that involve all lithotypes.

Figure 3. Mesostructural features of the *Lago della Vecchia* metagranite and associated rocks

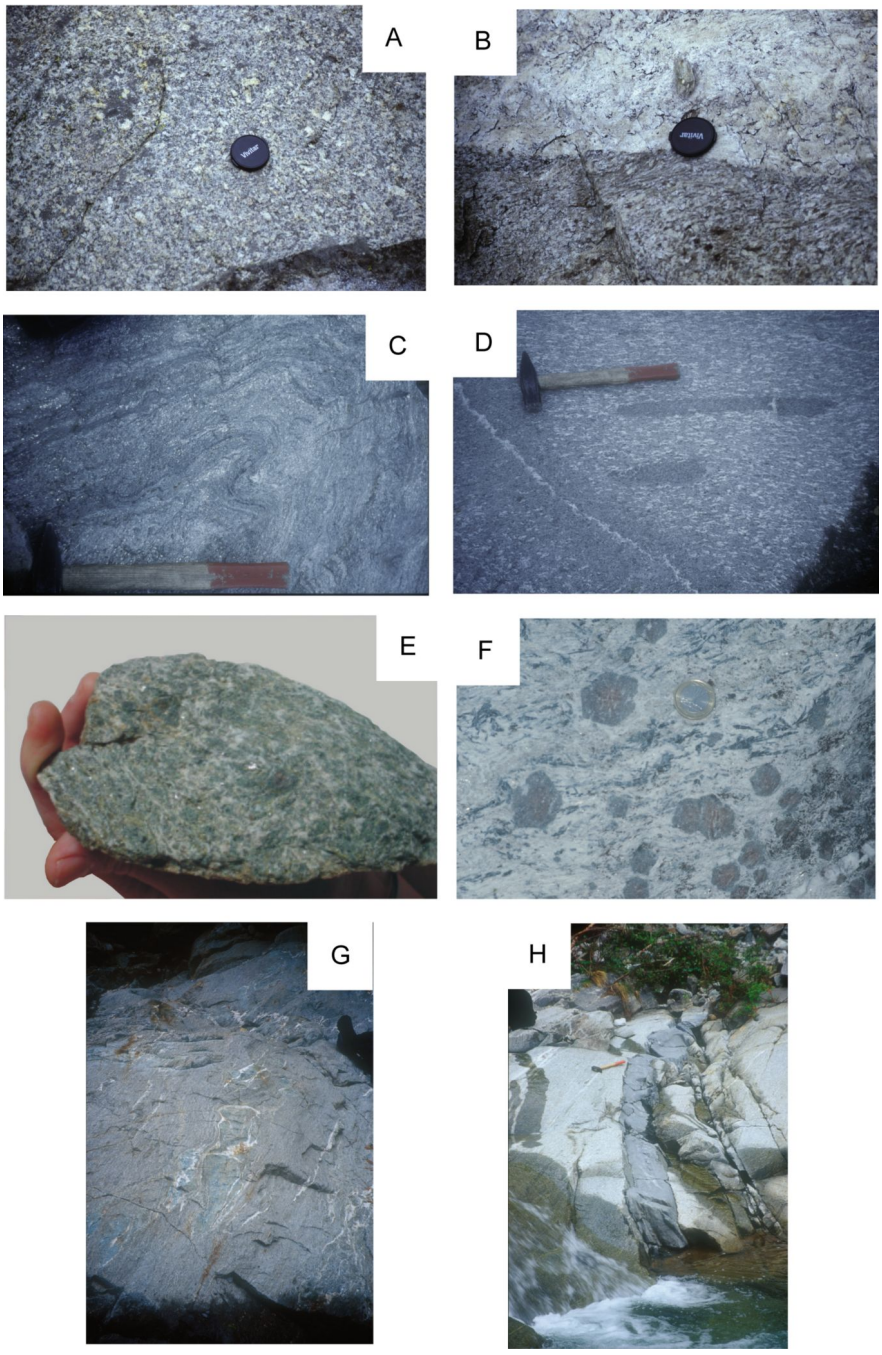

A) coronitc metagranite preserving igneous textures and mineralogy. Cm-sized K-feldspar crystals and mm-sized biotite are visible in the photograph. Pale-brown aggregates corresponds to plagioclase crystals replaced by aggregates of epidote and white mica. B) Localised shear zone occurring within the metagranite body along lithological contact with leucocratic granite. S-C foliations develop in few centimeters within the undeformed granite. C) Within deformed metagranites the foliation marked by shape preferred orientation of white mica, omphacite and quartz is locally folded. D) Dark, centimeter-sized stretched enclaves in mylonitic metagranite. The mylonitic foliation in the metagranite is marked by shape preferred orientation of quartz, white mica and omphacite, while it is marked by omphacite and glaucophane in the enclaves. E) Omphacite, garnet, white mica epidote eclogite. F) Garnet-bearing leucocratic metagranite. Cm-sized garnet show mm-sized corona of glaucophane; glaucophane mm-sized crystals form aggregates slightly oriented parallel to the foliation. G) Metre-sized eclogite boudins within deformed metagranite. H) Andesitic dykes crosscutting foliated metagranite.

Microstructural Analysis

We will focus on coronitic microstructures developed over the Mag0 parageneses aiming to reconstruct the microstructural and chemical evolution of igneous microdomain during the Alpine evolution. At macro- and microscopic scale, four igneous microdomains have been distinguished: biotite (Bt_I), white mica (Wm_I), plagioclase (Pl_I), K-feldspar (Kfs_I). Each microdomain is characterized by the development of peculiar microtextures and mineral assemblages during the Alpine evolution (Figs. 4, 5, 6).

Igneous biotite microdomain (Bt_I)

Bt_I occurs as 0.5-5 mm sized single crystals or aggregates of grains of low relief. Bt_I exhibits red-brown colours with a pleochroism from brown to reddish brown, tabular (001) habit and pseudo-hexagonal outline. Inner part of crystals are darker whereas rims are lighter (Fig. 4). Bt_I may be in contact with Qtz, Pl_I and Wm_I.

The boundaries between Bt_I and quartz do not show any corona or reaction rims, whereas coronas develop at the boundaries between Bt_I and Pl_I (Fig. 4b,d,e,f); Bt_I-Pl_I boundaries are delimited by a continuous corona of Grt_I (Fig. 4a-f). Toward Bt_I grains, Grt_I corona is associated with grains of about 30-50 µm of white mica (Wm_{II}) and pale brown Bt_{II}, defining a composite corona; correspondingly, toward Pl_I microdomains Grt_I is associated with aggregates of < 10µm of Wm_{II} (Fig. 4b-f). Grt_I is cleaner towards Pl_I microdomain than toward Bt_I (Fig. 4b, c). This feature is clear at BSE images (Fig. 4e,f) where the darker part of the Grt_I corona is always the one towards the Pl_I microdomains, where it is in contact with Wm_{II}; the lighter part of the corona always face toward Bt_I microdomains associated with large Wm_{II} crystals. Grt_I growing on the Bt_I side are also characterized by inclusions of Qtz.

Igneous white mica microdomain (Wm_I)

Wm_I occurs as single crystals (Fig. 4g,h) of 0.2–1 mm, showing perfect cleavage (001). Undulose extinction occurs (Fig. 4g,h) and it is often associated with a gentle folding of the Wm_I grains. Wm_I crystals are surrounded by thin aggregates of Wm_{II}. Where Wm_I is in contact with Pl_I, corona of Wm_{II} and Grt_I develop: they are similar to the ones observed between Bt_I and Pl_I (Fig. 4h). Wm_{II} close to the Wm_I crystals have a coarser grain-size than Wm_{II}-aggregates at the Wm_I-Pl_I microdomain boundaries (Fig. 4g).

Igneous plagioclase microdomain (Pl_I)

Pl_I is not preserved but corresponding pseudomorphic assemblages are easily distinguished by their meso- and microscopic shape and mineral association (Fig. 4a,b,d,e). Pl_I microdomains are several mm in their size and have rectangular shapes; they are constituted by fine-grained aggregates of Ep_I + Wm_{II} + Pl_{II} ± Grt_I (Fig. 4) that replace the cores of Pl_I. Pl_I rims are characterised by coarse grained aggregates of Wm_{II} at the Pl_I-Bt_I and Pl_I-Wm_I boundaries (Fig. 5f). Fine-grained aggregates of Ep_I + Wm_{II} + Pl_{II} + Grt occur at the Pl_I-Kfs_I microdomain boundaries (Fig. 5b-d).

Igneous k-feldspar microdomain (Kfs_I)

Several cm-thick Kfs_I microdomains are preserved (Fig. 3a). Kfs_I occurs as single crystals characterized by tartan twinning (Fig. 5d), deformation bends and undulose extinction (Fig. 5e). Kfs_I is fractured and partially replaced by aggregates of Pl_{II} (Ab). Coarse-grained (0.5-1 mm) Pl_{II} typically replaces Kfs_I from rims (Fig. 5d) or within fractures and forms aggregates of several mm. Pl_{II} may show simple or polysynthetic twinning. Fine-grained (< 50µm) Wm_{II} + Pl_{II} define corona between Kfs_I and Pl_I microdomains. Moreover, several mm to cm sized igneous allanite (Aln_I) occurs within coronitic metagranites (Fig. 5g,h). Aln_I is characterized by chemical zoning and it is often associated with igneous Ttn (Fig. 5g).

Summary of microstructural analysis

The excellent preservation of the geometry of the igneous microdomain, as well locally mineralogy, allowed definition of the reactions that occurred at specific domain boundaries and reconstruction of the primary igneous assemblage, constituted by: Bt_I + Wm_I + Qtz + Kfs + Pl_I ± Aln ± Ttn. At the boundaries between Bt_I and Pl_I microdomains, two coronas develop: 1) Bt_{II} + Wm_{II} + Grt_I; 2) Wm_{II} + Grt_I. The Wm_{II} + Grt_I + Ep + Ab aggregates occur between Wm_I and Pl_I and Kfs_I – Pl_I microdomains and pseudomorphically replace Pl_I cores. The Kfs_I cores are partly to completely substituted by Ab from the Pl_I - Kfs boundaries or along fractures.

Figure 4. Microphotographs

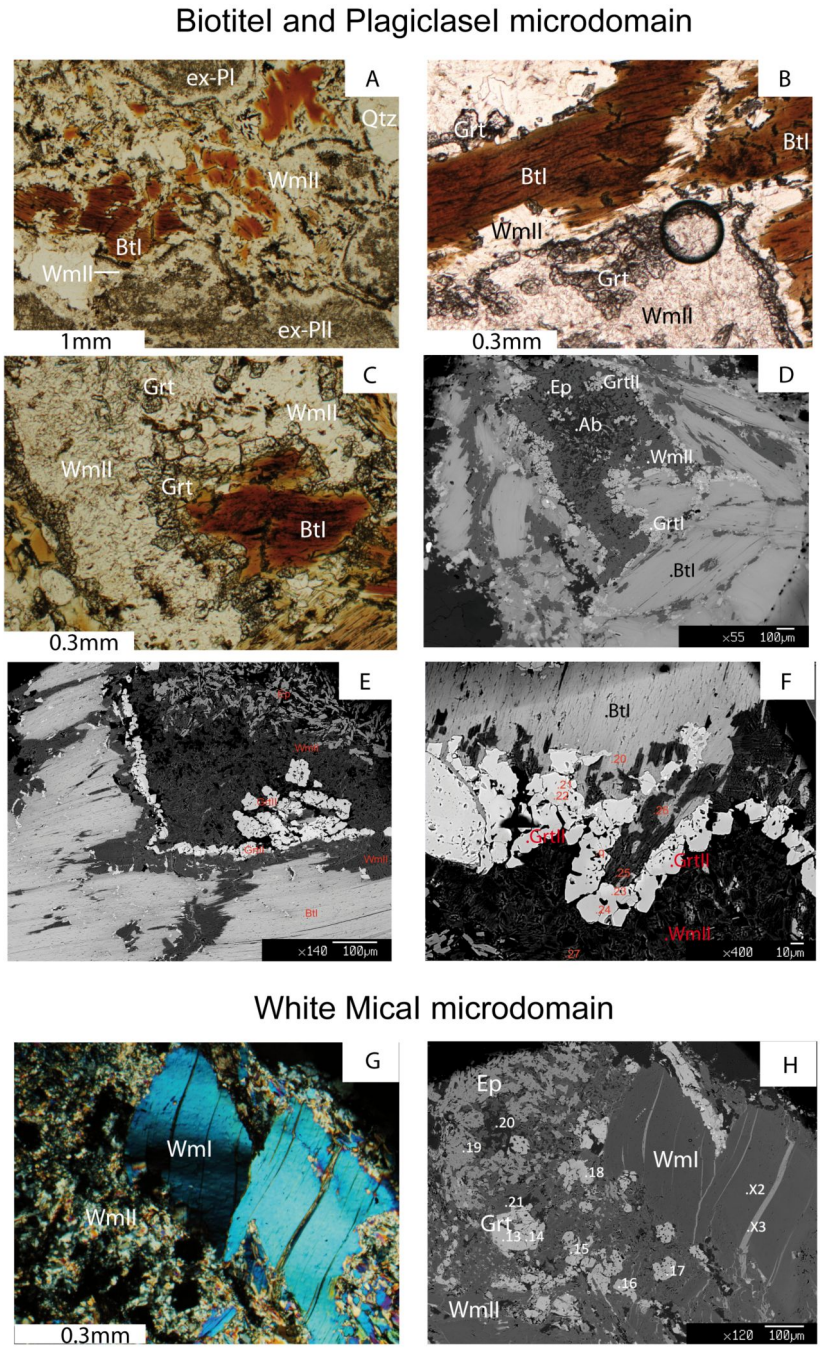

A) Igneous biotite, plagioclase, white mica and quartz microdomains are well distinguishable: igneous plagioclase is replaced by fine-grained aggregates with high relief. The boundaries between ex-plagioclase and Bt_I microdomains are marked by continuous Grt_I + Wm_{II} corona. B and C) Details of the Grt_I + Wm_{II} corona at the boundary Bt_I-Pl_I. D, E and F) BSE-SEM image of Bt_I – Pl_I microdomain. A continuous corona of garnet defines the boundary between Bt_I and original igneous plagioclase. Wm_{II} grows in association with epidote and albite in plagioclase. Garnet shows clear zoning: the inner part, Bt_I-facing, is lighter and rich in quartz inclusions; the external part, Pl_I-facing, is darker and clean. G) Wm_I surrounded by thin aggregates of Wm_{II}. H) BSE-SEM of the Wm_I microdomain associated with aggregates of Wm_{II} + Grt + Ep + Ab.

Figure 5. Microphotographs

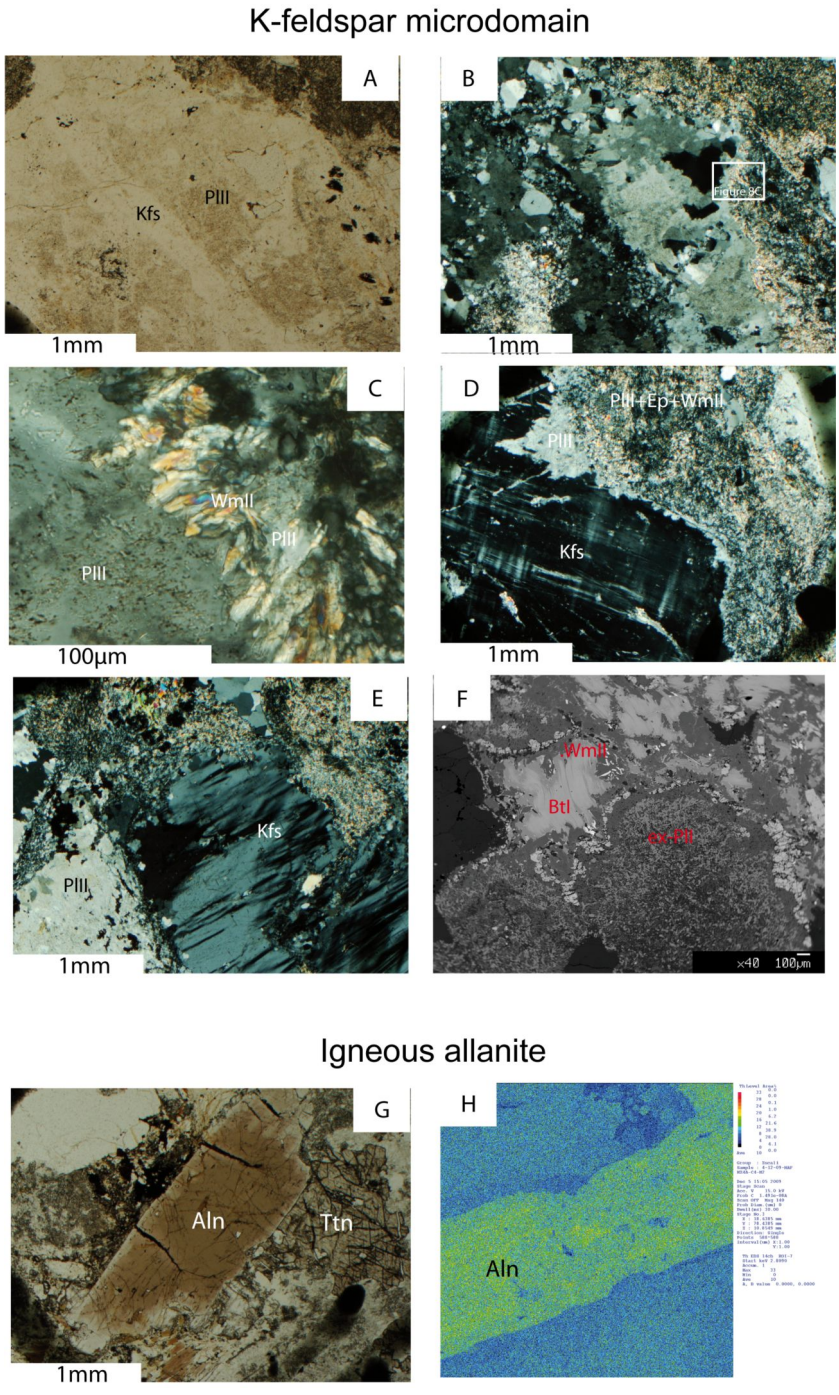

A) Plane polarized light image of large K-feldspar site partially substituted by a pale-brown aggregate of albite. B) Image A - crossed polars. C) Detail of B; fine-grained aggregates of Wm_{II} associated with fine grained Ab that replace Pl_I; left side of the microphotograph is occupied by large Pl_{II} (Ab) aggregates substituting Kfs megacrystals. D) Kfs megacrystals characterized by tartan twinning partially substituted by aggregates of Pl_{II} (Ab) at the rims. Right side of the microphotograph: fine-grained aggregate of Pl_{II}+Ep+Wm_{II} substituting the Pl_I microdomains. E) Large crystals of Kfs with undulose extinction and Pl_{II} aggregates. F) BSE-SEM image of Pl_I microdomain completely substituted by aggregates of Pl_{II}+Wm_{II} +Ep±Qtz and crystals of Bt_I rimmed by Bt_{II} and Wm_{II} crystals. G) Igneous allanite in contact with igneous titanite. Aln is characterized by zoning from brown core to pale-brown, colorless rims. H) X-ray map image showing the distribution of Th in the igneous allanite.

Mineral chemistry

X-Ray maps and minerals were analysed (Table 1) with an Electron Microprobe (EPMA) and a Scanning Electron Microscope (SEM) at the Dipartimento di Scienze della Terra "A. Desio" – Università degli Studi di Milano. The operating conditions were 20kV accelerating voltage, filament intensity 1.70A and probe intensity of 280pA. Beam sizes were < 1µm, 4µm and 10µm. Natural silicates were used as standards and matrix corrections were calculated with ZAF (Z=atomic number, A=absorption, F=fluorescence) procedure.

The relative chronology used for mineral phases (e.g. Bt_I and Bt_{II}; Wm_I and Wm_{II}) is inferred from microstructural analysis and thus only corresponds to the microstructural sites occupied by each group of minerals, their textures, microstructures and optical properties. The inferred chronology does not necessarily correspond to differences in chemical composition.

In this paragraph mineral phases chemical compositions are discussed with respect to the microstructural relative chronology, to check the occurrence of the expected chemical variation.

Figure Table 1. Selected chemical compositions for principal mineral phases, separated on the basis of their microstructural position.

Sample	MZ1B-C2-X4	MZ1B-C3-X5	MZ1B-C3-X8	MZ1B-C4-X12	MZ4A-C4-Y5	MZ4A-C4-Y6	MZ1a-C1-10	MZ1a-C1-18	MZ1a-C2-19	MZ1a-C2-20	MZ1a-C2-34	MZ1a-C2-45	MZ1B-C3-X9
Mineral	Bt1	Bt1	Bt1	Bt1	Bt1	Bt1	Bt1	Bt1	Bt1	Bt1	Bt1	Bt1	Bt2
SiO2	38.37	37.42	37.79	37.95	38.58	38.8	37.5	37.98	39.14	38.84	38.5	38.52	38.94
TiO2	3.56	4.37	4.82	4	3.74	2.33	3.34	3	3.92	2.86	2.73	2.38	1.69
Al2O3	13.54	14.58	13.9	13.94	13.58	13.78	15.82	15.25	13.93	14.86	14.62	14.29	14.75
FeO	23.8	24.5	24.37	24.37	24.55	24.12	24.07	24.35	23.64	23.48	24.2	23.86	22.5
MnO	0.299	0.305	0.342	0.316	0.297	0.277	0.32	0.297	0.28	0.313	0.322	0.328	0.284
MgO	8.21	7.03	6.92	7.44	7.37	8.32	7.26	7.96	8.02	8.33	8.46	8.82	9.14
CaO	0.045	0.068	0.011	0.042	0.02	0.068	0.014	0.008	0	0.033	0.041	0.187	0.051
Na2O	0.031	0.03	0.015	0.031	0.026	0.045	0.044	0.044	0.03	0.047	0.045	0.061	0.051
K2O	9.43	9.59	9.75	9.52	9.54	8.99	9.52	9.51	8.72	9.66	8.91	7.45	9.27
Sum	97.29	97.89	97.92	97.61	97.70	96.73	97.89	98.40	97.68	98.42	97.83	95.90	96.68
Ox	***22***	***22***	***22***	***22***	***22***	***22***	***22***	***22***	***22***	***22***	***22***	***22***	***22***
Si	5.841	5.692	5.748	5.780	5.866	5.923	5.676	5.722	5.884	5.820	5.808	5.874	5.900
Ti	0.408	0.500	0.551	0.458	0.428	0.268	0.380	0.340	0.443	0.322	0.310	0.273	0.193
Al	2.429	2.614	2.492	2.502	2.433	2.479	2.822	2.708	2.468	2.624	2.599	2.568	2.634
Fetot	3.030	3.116	3.100	3.104	3.121	3.079	3.047	3.068	2.971	2.942	3.053	3.042	2.851
Mn	0.039	0.039	0.044	0.041	0.038	0.036	0.041	0.038	0.036	0.040	0.041	0.042	0.036
Mg	1.863	1.594	1.569	1.689	1.671	1.893	1.638	1.788	1.797	1.861	1.903	2.005	2.065
Ca	0.007	0.011	0.002	0.007	0.003	0.011	0.002	0.001	0.000	0.005	0.007	0.031	0.008
Na	0.009	0.009	0.004	0.009	0.008	0.013	0.013	0.013	0.009	0.014	0.013	0.018	0.015
K	1.831	1.861	1.892	1.850	1.850	1.751	1.838	1.828	1.672	1.847	1.715	1.449	1.792
CatSUM	15.457	15.436	15.403	15.440	15.419	15.452	15.458	15.505	15.280	15.475	15.447	15.303	15.494
AlIV	2.159	2.308	2.252	2.220	2.134	2.077	2.324	2.278	2.116	2.180	2.192	2.126	2.100
AlVI	0.270	0.306	0.240	0.282	0.299	0.402	0.498	0.430	0.351	0.445	0.407	0.442	0.534
T(°C)_H2005	***695***	***720***	***733***	***709***	***698***	***625***	***681***	***665***	***706***	***659***	***651***	***631***	***565***
FeO.calc	21.34	22.69	22.71	22.20	22.18	20.93	22.19	22.08	21.26	21.26	21.39	20.19	19.64
Fe2O3.calc	2.71	1.99	1.83	2.39	2.61	3.51	2.07	2.50	2.62	2.44	3.09	4.04	3.14
Fe3	0.308	0.227	0.208	0.272	0.296	0.399	0.235	0.282	0.295	0.274	0.348	0.459	0.355
Fe2	2.698	2.872	2.875	2.811	2.802	2.648	2.794	2.764	2.655	2.648	2.678	2.548	2.470

Sample	MZA1									
Mineral	WmI	WmI	WmII_C_Pl	WmII_C_Pl	WmII_C_Pl	WmII_BtI	WmII_BtI	WmII_WmI	WmII_WmI	wmII_F_Pl
SiO2	47.70	49.51	50.27	49.87	50.80	49.45	50.18	50.61	50.65	51.02
TiO2	0.90	0.05	0.13	0.14	0.04	0.16	0.12	1.72	1.62	0.06
Al2O3	32.21	26.25	26.52	30.13	25.98	26.43	28.43	26.07	25.05	25.63
FeO	1.92	6.13	2.58	2.47	4.69	6.64	5.38	2.40	2.45	2.97
MnO	0.00	0.03	0.00	0.00	0.05	0.10	0.06	0.01	0.00	0.00
MgO	1.30	1.34	1.96	2.18	3.12	3.17	2.86	3.63	3.41	2.53
CaO	0.01	0.01	0.01	0.00	0.02	0.07	0.00	0.04	0.01	0.00
Na2O	0.14	0.06	0.12	0.07	0.05	0.05	0.07	0.06	0.06	0.09
K2O	11.27	11.10	11.25	10.79	10.47	10.58	11.09	11.20	11.29	11.15
OxSum	95.45	94.47	92.83	95.65	95.23	96.64	98.19	95.73	94.54	93.44
Ox	***22***	***22***	***22***	***22***	***22***	***22***	***22***	***22***	***22***	***22***
Si	6.377	6.817	6.913	6.63	6.858	6.671	6.62	6.766	6.861	6.977
Ti	0.09	0.005	0.013	0.014	0.004	0.016	0.012	0.173	0.165	0.006
Al	5.075	4.259	4.298	4.721	4.134	4.202	4.42	4.108	3.999	4.13
Fetot	0.215	0.706	0.297	0.275	0.529	0.749	0.594	0.268	0.277	0.34
Mn	0	0.004	0	0	0.006	0.011	0.006	0.001	0	0
Mg	0.259	0.275	0.402	0.432	0.628	0.638	0.563	0.724	0.689	0.516
Ca	0.002	0.001	0.001	0	0.003	0.01	0	0.005	0.001	0
Na	0.036	0.016	0.031	0.017	0.013	0.013	0.018	0.015	0.014	0.023
K	1.922	1.949	1.973	1.83	1.803	1.821	1.866	1.91	1.951	1.945
CatSUM	13.975	14.031	13.927	13.919	13.979	14.13	14.1	13.969	13.957	13.936
AlIV	1.62	1.18	1.09	1.37	1.14	1.33	1.38	1.23	1.14	1.02
AlVI	3.45	3.08	3.21	3.35	2.99	2.87	3.04	2.87	2.86	3.11

Sample	MZ1B-C2-14	MZ1B-C2-15	MZ1B-C2-16	MZ1B-C2-18	MZ1B-C3-27	MZ1B-C3-28	MZ1a-C2-21	MZ1a-C2-24	MZ1a-C2-47	MZ1B-C7-62	MZ1B-C7-64	MZ4A-C1-8	MZ4A-C3-25	MZ4A-C3-26	MZ1a-C1-14
Mineral	Grtl@Wml	Grtl@Wml	Grtl@Wml	Grtl@Wml	Grtl@Btl-**Pll**	Grtl@**Btl**-Pll	Grtl@**Btl**-Pll	Grtl@Btl-**Pll**	Grtl@**Btl**-Pll	Grtl@**Btl**-Pll	Grtl@Pll	Grtl@Kfsl-Wml	Grtl@Kfsl-Wml	Grtl@Kfsl-Wml	Grtl@Btl
TiO2	0.18	0.02	0.12	0.21	0.07	0.02	0.17	0.02	0.21	0.12	0.13	0.00	0.02	0.08	0.27
SiO2	37.09	37.39	37.94	37.52	37.79	37.53	37.42	38.22	37.32	37.01	37.67	37.77	38.23	37.60	37.21
Al2O3	21.43	21.42	21.60	21.55	21.48	21.25	21.33	21.53	21.49	21.40	21.78	21.14	20.81	21.22	21.85
FeO	31.08	23.55	23.20	26.77	22.78	34.75	31.57	21.49	28.99	31.56	22.01	21.44	24.93	25.31	32.30
MnO	0.42	0.46	0.34	0.47	0.44	0.96	0.80	0.39	1.32	0.44	0.53	0.67	0.33	0.44	1.29
MgO	2.49	0.81	1.19	1.58	0.72	2.84	2.83	0.71	2.35	3.14	0.93	0.51	0.63	0.93	2.56
CaO	7.49	15.87	15.90	12.09	16.63	3.49	6.04	17.62	8.16	6.42	16.99	17.95	14.64	14.31	5.42
Na2O	0.04	0.01	0.05	0.05	0.02	0.01	0.03	0.02	0.10	0.03	0.04	0.01	0.00	0.03	0.02
K2O	0.01	0.04	0.02	0.05	0.05	0.03	0.02	0.03	0.04	0.00	0.05	0.00	0.01	0.02	0.01
Sum	100.23	99.56	100.35	100.28	99.97	100.87	100.21	100.02	99.98	100.13	100.14	99.49	99.61	99.95	100.93
Ox	12	12	12	12	12	12	12	12	12	12	12	12	12	12	12
Ti	0.011	0.001	0.007	0.012	0.004	0.001	0.010	0.001	0.012	0.007	0.008	0.000	0.001	0.005	0.016
Si	2.948	2.962	2.973	2.963	2.977	2.988	2.978	3.000	2.966	2.940	2.954	2.986	3.037	2.978	2.949
Al	2.007	1.999	1.995	2.005	1.994	1.994	2.000	1.992	2.013	2.003	2.013	1.970	1.948	1.981	2.041
Fetot	2.066	1.560	1.520	1.768	1.500	2.314	2.101	1.411	1.927	2.096	1.443	1.417	1.656	1.676	2.141
Mn	0.028	0.031	0.022	0.031	0.029	0.065	0.054	0.026	0.089	0.029	0.035	0.045	0.022	0.030	0.086
Mg	0.295	0.096	0.138	0.186	0.084	0.337	0.336	0.083	0.278	0.372	0.109	0.060	0.075	0.110	0.302
Ca	0.638	1.347	1.335	1.023	1.403	0.298	0.515	1.482	0.695	0.546	1.427	1.520	1.246	1.214	0.460
Na	0.007	0.001	0.008	0.007	0.003	0.001	0.004	0.003	0.015	0.005	0.007	0.001	0.001	0.004	0.003
K	0.001	0.004	0.002	0.005	0.005	0.003	0.002	0.003	0.005	0.000	0.005	0.000	0.001	0.002	0.001
cationSUM	8.028	8.027	8.018	8.019	8.017	8.010	8.010	8.004	8.017	8.036	8.026	8.020	7.988	8.020	8.011
Alm	68.25	51.43	50.41	58.77	49.73	76.78	69.90	47.01	64.46	68.87	47.87	46.58	55.22	55.31	71.60
Py	9.75	3.15	4.59	6.17	2.79	11.19	11.17	2.75	9.32	12.22	3.61	1.98	2.49	3.64	10.12
Grs	21.07	44.40	44.26	34.01	46.52	9.88	17.13	49.38	23.25	17.95	47.35	49.97	41.54	40.07	15.39
Spss	0.93	1.01	0.74	1.05	0.96	2.15	1.80	0.86	2.97	0.97	1.17	1.47	0.75	0.98	2.89
Fe2+	*2.03*	*1.52*	*1.49*	*1.75*	*1.48*	*2.30*	*2.09*	*1.40*	*1.92*	*2.05*	*1.42*	*1.37*	*1.61*	*1.64*	*2.14*
Fe3+	*0.034*	*0.038*	*0.025*	*0.020*	*0.025*	*0.017*	*0.011*	*0.007*	*0.009*	*0.049*	*0.026*	*0.044*	*0.047*	*0.037*	*0.000*

Mineral	Kfs	PlII_Ab	PlII_Ab	Ttn_ign	Ttn2_btI
SiO2	65.67	68.89	68.43	31.31	31.77
TiO2	0.006	0	0.025	36.22	23.87
Al2O3	18.9	19.09	19.5	2.35	11.35
FeO	0.022	0.016	0.057	0.198	0.972
MnO	0	0.041	0	0.033	0.018
MgO	0.005	0.001	0	0.005	0.094
CaO	0	0.056	0.218	28.92	28.74
Na2O	0.571	11.67	11.77	0.011	0.002
K2O	15.36	0.085	0.312	0.001	0.129
Sum	100.535	99.848	100.311	99.048	96.945
Ox	***8***	***8***	***8***	**10**	**10**
Si	3	3.012	2.987	2.054	2.099
Ti	0	0	0.001	1.787	1.186
Al	1.017	0.983	1.003	0.182	0.884
Fetot	0.001	0.001	0.002	0.011	0.054
Mn	0	0.002	0	0.002	0.001
Mg	0	0	0	0.001	0.009
Ca	0	0.003	0.01	2.032	2.034
Na	0.051	0.989	0.996	0.001	0
K	0.895	0.005	0.017	0	0.011
CationSUM	4.964	4.994	5.017	6.069	6.278

Sample	MZ5B-C1-2	MZ5B-C1-3	MZ5B-C1-5	MZ5B-C2-12	MZ5B-C4-37	MZ5B-C4-38	MZ1B-C2-19	MZ1B-C6-56
an.	Ep_Zo	Ep_Zo	Ep	Ep	Ep	Ep	Ep	Ep
K2O	0.04	0.01	0.04	0.00	0.00	0.01	0.01	0.01
CaO	22.43	22.49	22.78	22.71	23.74	23.15	23.61	23.50
TiO2	0.01	0.00	0.00	0.00	0.01	0.00	0.02	0.07
Cr2O3	0.00	0.00	0.00	0.00	0.00	0.00	0.00	0.00
MnO	0.02	0.00	0.12	0.04	0.05	0.09	0.08	0.11
FeOt	0.83	0.80	6.70	0.79	1.51	10.10	11.33	9.18
NiO	0.00	0.00	0.00	0.00	0.00	0.00	0.00	0.00
Na2O	0.03	0.03	0.00	0.01	0.02	0.01	0.00	0.03
SiO2	39.75	40.37	39.03	40.23	40.30	38.78	38.54	38.68
Al2O3	32.77	33.27	27.70	32.28	32.14	25.22	24.56	25.74
MgO	0.01	0.00	0.02	0.00	0.00	0.01	0.02	0.01
TOTAL	95.88	96.97	96.40	96.06	97.76	97.37	98.16	97.33
formula: 8 cations and 12.5 oxygens, Fe3+=3-Alvi-Ti-Cr								
Si	3.080	3.093	3.064	3.115	3.071	3.045	3.011	3.030
Al.IV	0.000	0.000	0.000	0.000	0.000	0.000	0.000	0.000
Al.VI	2.994	3.005	2.564	2.946	2.888	2.335	2.262	2.377
Ti	0.001	0.000	0.000	0.000	0.000	0.000	0.001	0.004
Cr	0.000	0.000	0.000	0.000	0.000	0.000	0.000	0.000
Fe3+	0.006	0.000	0.436	0.051	0.096	0.663	0.737	0.601
Fe2+	0.048	0.051	0.004	0.000	0.000	0.000	0.004	0.000
Mg	0.001	0.000	0.003	0.000	0.000	0.001	0.002	0.001
Ni	0.000	0.000	0.000	0.000	0.000	0.000	0.000	0.000
Mn	0.001	0.000	0.008	0.003	0.003	0.006	0.005	0.007
Ca	1.862	1.846	1.916	1.884	1.939	1.948	1.977	1.973
Na	0.004	0.005	0.001	0.001	0.003	0.001	0.000	0.004
K	0.004	0.001	0.004	0.000	0.000	0.001	0.001	0.001
FeO	0.74	0.80	0.06	-	-	-	0.06	-
Fe2O3	0.10	-	7.38	0.88	1.68	11.22	12.53	10.20
Total.calc	95.89	96.97	97.13	96.15	97.93	98.49	99.41	98.35
%pist.	0.20	0.00	14.53	1.71	3.23	22.12	24.55	20.16
a.zo/czo	0.99	1.00	0.56	0.95	0.89	0.33	0.26	0.38

Biotite (Bt)

Igneous biotites (Bt_I in Figs. 4, 6, 7, Table 1 are characterized by high Ti content that ranges from 0.30 to 0.55 a.p.f.u. Ti content intervals correspond to Mg contents ranging from 1.89 to 1.57 a.p.f.u. Fe^{tot} (all Fe as Fe^{2+}) ranges from 3.00 to 4.22 a.p.f.u. and Al^{VI} from 0.20 to 0.40 a.p.f.u. (Table 1). These chemical intervals (Fig. 7) correspond to igneous composition (Deer *et al.* 1996).

Bt_{II} corresponds to the darker parts of Bt_I grains in BSE images (Fig. 4, Fig. 7) or generally to the rims of Bt_I grains; Bt_{II} is generally enriched in Mg and poorer in Ti with respect to Bt_I (Fig 7). These trends are well described in Fig. 7 where the Ti vs. Mg diagram shows this continuous relation.

Figure 6. Schematic and Panoramic views

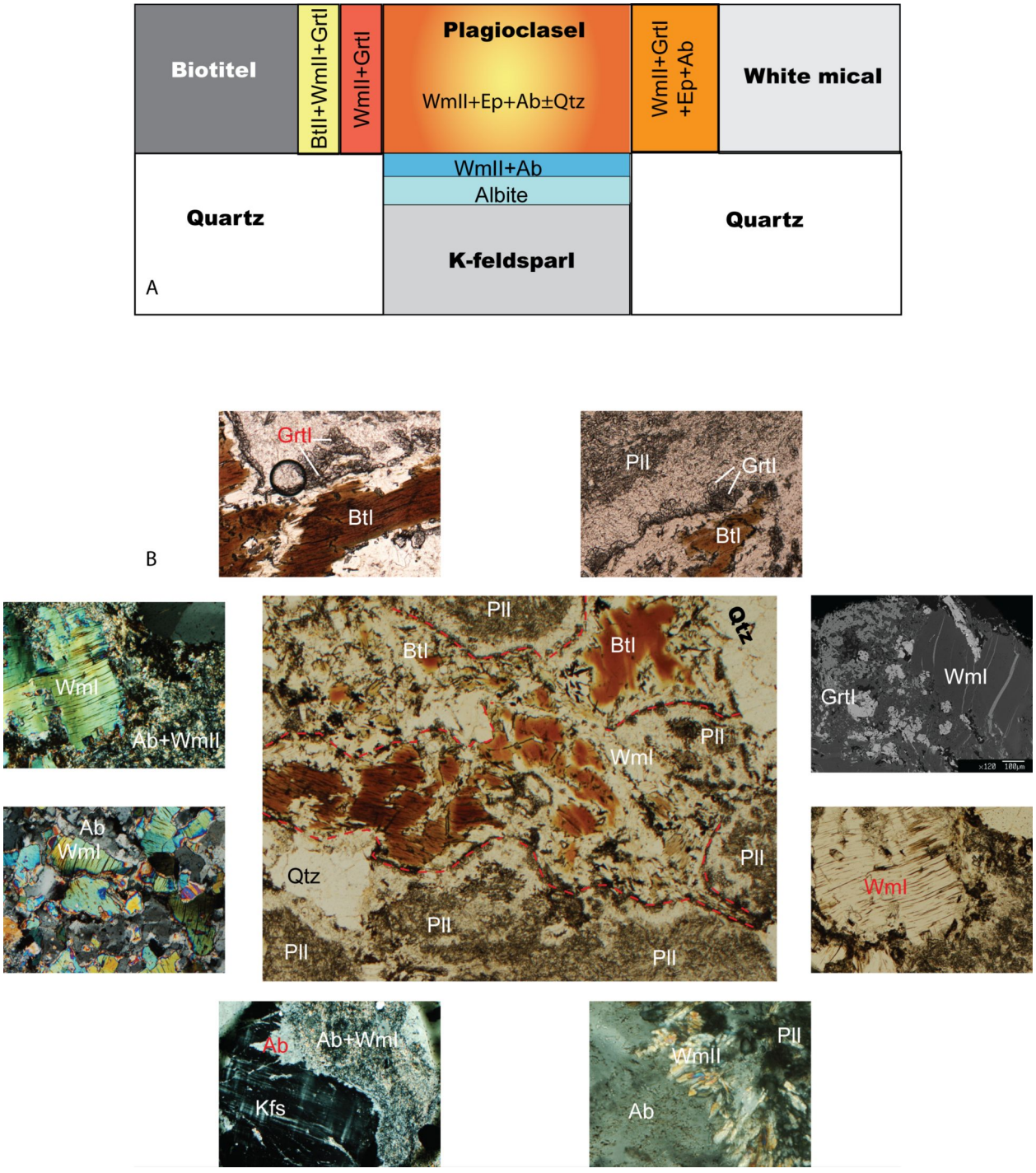

A) Schematic view of the igneous microdomain and their main features during the post-igneous transformations inferred from microstructural analysis. B) Panoramic view of the relations between igneous microdomains and Alpine coronas with details for each specific microstructure and mineral assemblage. Red dashed lines indicate inferred grain boundaries between igneous minerals.

Figure 7. Diagrams showing the Biotite and Garnet chemical compositions and variations with respect to their positions within corona textures.

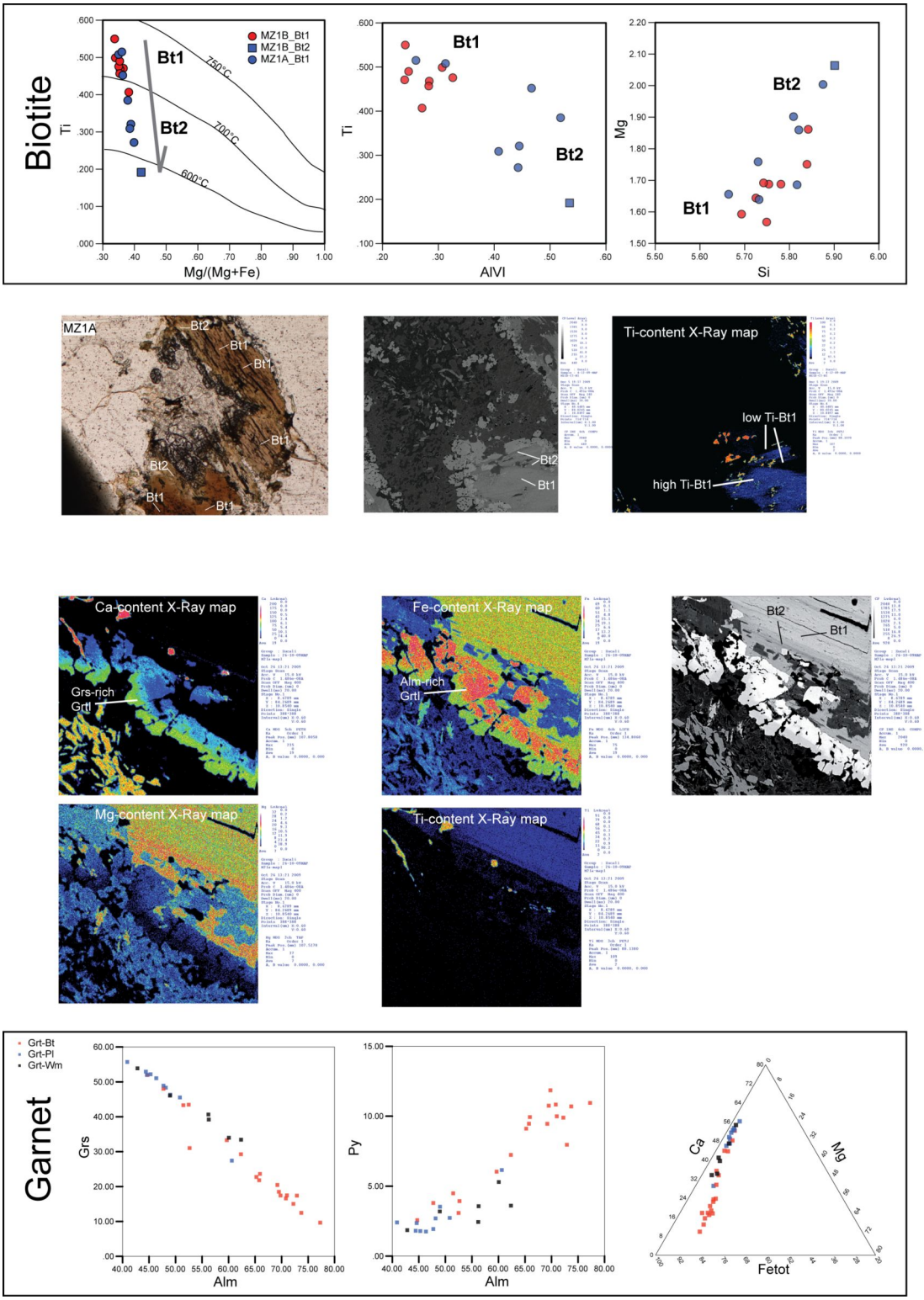

Ti vs. Mg/(Mg+Fe) diagram of biotites also shows the evolution from high-temperature Bt_I to lower-temperature Bt_{II} as described by Henry *et al.* (2005). Color-enhanced X-ray maps show the distribution of Ca, Fe, Mg and Ti in the reaction corona between Pl_I and Bt_I.

Figure 8. Compositional diagrams of white mica and epidote. A) Compositional diagrams of white mica and epidote showing the compositional variations of the mineral phases with respect to the occupied positions as displayed in

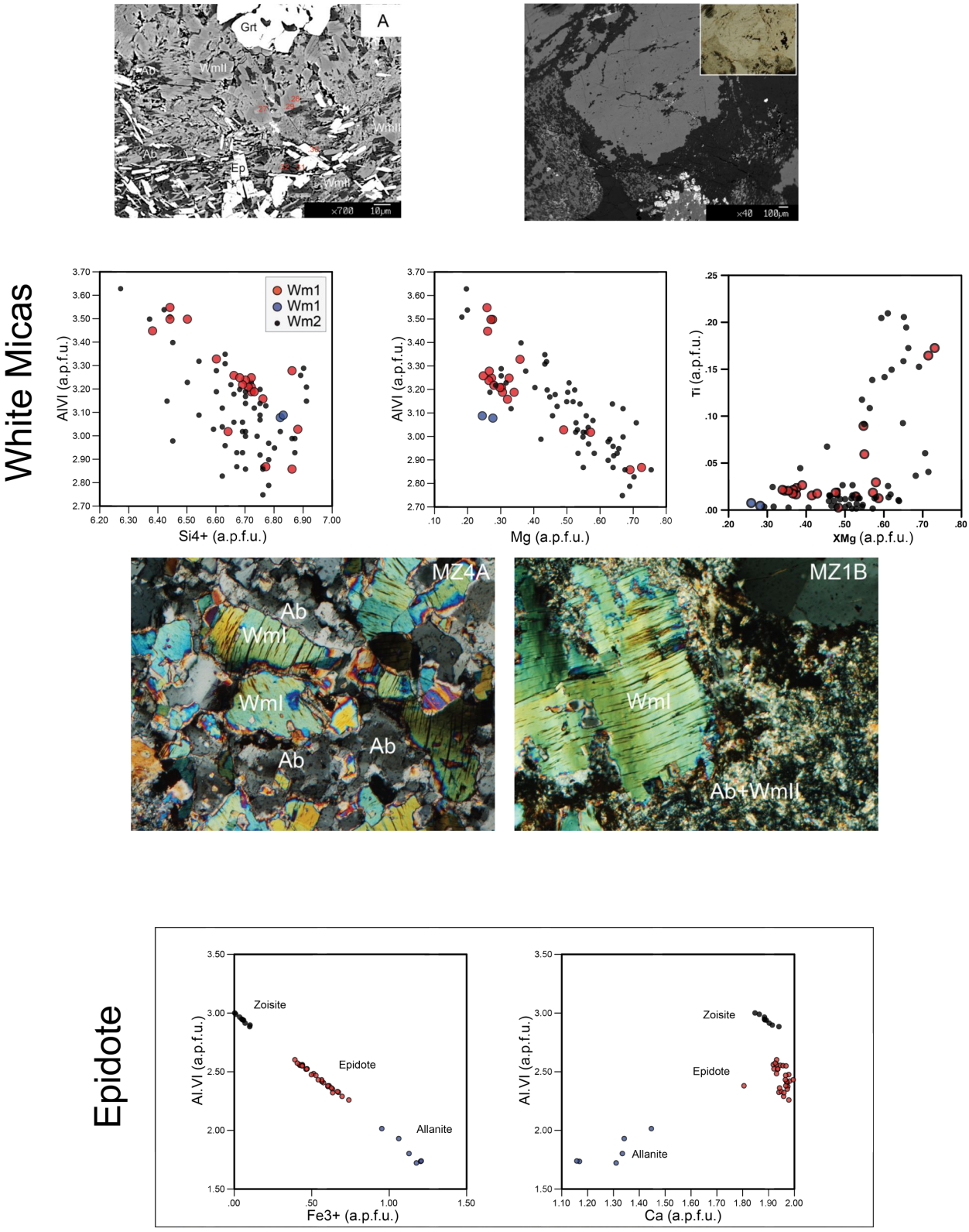

BSE-SEM images and microphotographs.

White Mica (Wm)

Wm_I is phengitic mica and displays a wide range in composition: Si content varies from 6.38 to 6.88 a.p.f.u., Al^{VI} from 2.86 to 3.55 a.p.f.u., Fe^{tot} from 0.18 to 0.70 a.p.f.u. and Mg from 0.25 to 0.72 a.p.f.u. These chemical variations do not correspond to a regular zoning within Wm_I grains.

Wm_{II} is phengitic mica and is characterized by continuous compositional ranges for Si content, from 6.30 to 6.95 a.p.f.u., Al^{VI} content, from 2.75 to 3.65 a.p.f.u., Fe^{tot} content, from 0.2 to 0.78 a.p.f.u. and Mg content from 0.18 to 0.75 a.p.f.u. Wm_{II} grown within Pl_I pseudomorphic microdomains shows two stages of growth (Fig. 8), characterized by an increase in Mg and Fe^{tot} contents from core to rim, respectively > 0.45 a.p.f.u. and > 0.40 a.p.f.u. (Tab. 1).

Ti content varies from 0.0 to 0.20 a.p.f.u. and highest values are found in Wm_{II} within Pl_I microdomains as cores of lower Ti content Wm_{II} (Fig. 8).

Garnet (Grt)

The Grt_I composition is controlled by the growing microdomain and by the adjacent mineral phases.

Grt_I is Grs-rich (45-55 %) where it is in association with Wm_{II}, Ab and Ep within Pl_I microdomains (Fig. 4); in these Grt_I, Alm ranges from 40 to 50% and Pyp < 15% (Fig. 7). More complex is the compositional pattern of Grt_I defining corona between Wm_I or Bt_I and Pl_I micrdomains; X-ray maps (Fig. 7) show the sharp chemical variation of these corona: Bt_I-facing Grt_I is Ca-poor and Fe-rich while, oppositely, Pl_I-facing Grt_I is enriched in Ca and depleted in Fe. The composition of Grt_I grown towards Bt_I shows a Ca content that ranges from 0.30 to 1.00 a.p.f.u. Fe^{tot} varies from 1.80 and 2.34 a.p.f.u. (Fig. 7). Corresponding Grt_I growing towards Pl_I are characterized by Ca content from 1.20 to 1.70 a.p.f.u., Fe^{tot} from 1.25 and 1.80 a.p.f.u. Mg content in corona-Grt ranges from < 0.1 to 0.37 a.p.f.u. where highest contents are generally in Bt_I-facing Grt_I. Grt_I grown at the boundaries of Wm_I shows an intermediate composition: Ca ranges from 1.00 to 1.40 a.p.f.u., Fe^{tot} from 1.48 to 1.93 a.p.f.u. and Mg from 0.07 to 0.16 a.p.f.u. (Tab. 1). Fe^{3+} content for all Grt_I is commonly low, having maximum content of 0.07 a.p.f.u.

Feldspar (K-feldspar and plagioclase)

K content in K-feldspar is always > 0.8 a.p.f.u. while in Pl_{II} Na content is always > 0.90 a.p.f.u. Both Kfs and Pl_{II} have Ca content < 0.07 a.p.f.u.

Epidote (Ep)

Ep_I are Fe-rich epidote and zoisite (Fig. 8). Fe^{3+} content in epidote ranges from 0 to 1.47 a.p.f.u. that corresponds respectively to Al^{VI} content 0 to 1.6 a.p.f.u. In zoisite Fe^{3+} is < 0.2 a.p.f.u. and Al^{VI} content ranges from 2.8 to 3.0 a.p.f.u. (Tab. 1). Epidote corresponds to higher Fe^{3+} contents (0.3 – 0.75) and lower Al^{VI} (2.2 – 2.6).

Chlorite (Chl)

Fe^{tot} content in Chl varies from 5.00 to 5.94 a.p.f.u., Mg content from 3.20 to 4.01 and Al^{VI} from 2.37 to 2.67 a.p.f.u. (Tab. 1).

Titanite (Ttn)

Ti content in titanite varies from 1.78 in igneous titanite (Tab. 1) to 1.18 a.p.f.u. in metamorphic titanite. Al content varies from 0.13 to 0.89 a.p.f.u.

Chemical profiles

Figure 10 shows qualitative chemical profiles obtained from X-rays maps, using ImageJ (Rasband, 1997; Prenzel *et al.* 2009). Distances (i.e. abscissae) are in µm, while intensities are in count per seconds.

Fe and Ca contents profiles (Fig. 10) are characterized by a typical pattern that reflect to the microdomain geometry and the chemical partitioning due to the microstructural positions (Kohn, 2003). In particular the Grt_I profile at the boundary between Pl_I and Bt_I microdomains is commonly described by a low Fe content toward the Pl_I domain; the Fe content sudden increases and then decreases toward Bt_I. Ca content shows highest values at the boundaries with Pl_I, higher than Fe contents, quickly decreasing toward the middle of the grain and toward Bt_I. Ca and Fe profiles intersect at intermediate values and highest Fe and Ca contents are generally comparable (see mineral analyses).

Figure 9. Image analysis procedure

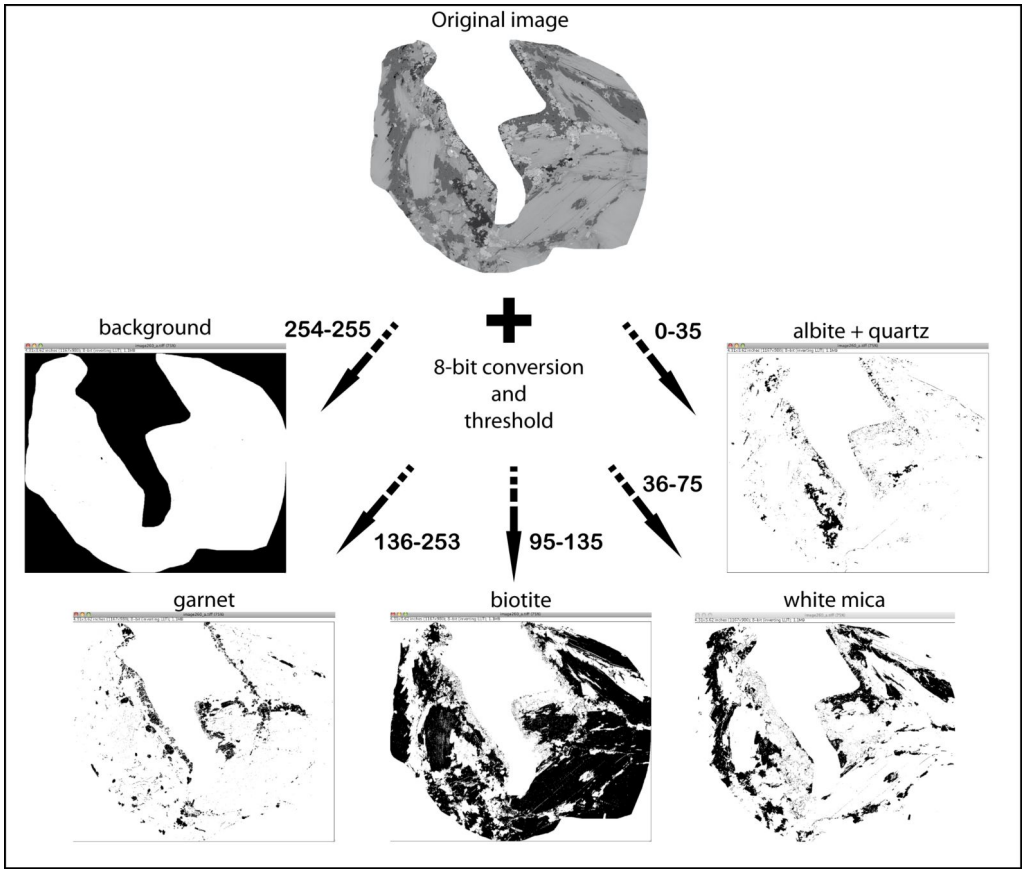

A) Image analysis procedure: from the original image, successive grey-scale thresholds intervals allow to define black-white images separating background (white), garnet, biotite, white mica and albite+quartz.

Such chemical relations allow to infer the most likely position of the former grain boundary between biotite and plagioclase, which may be located in correspondence of the fast decrease Fe and corresponding Ca content increase.

- Step 1)
  $Bt_I \rightarrow Bt_{II} + Wm_{II} + \text{Alm-rich } Grt_I$
  Pl_I stable
- Step 2)
  $Bt_I + Ca^{2+} (Pl_I) \rightarrow Bt_{II} + Wm_{II} + \text{Grs-rich } Grt_I$
  $Wm_I + Ca^{2+} (Pl_I) \rightarrow Wm_{II} + Grt$
  $Pl_I + H_2O + K^+ + Ti^{4+} + Mg^{2+} + Fe^{2+} \rightarrow Ab + Wm_{II} + Ep \pm Grt$
  $Pl_I \text{ rim} + H_2O + K^+ + Ti^{4+} + Mg^{2+} + Fe^{2+} \rightarrow Wm_{II} + Ab \pm Ep \pm Grt_I$
  $Pl_I \text{ core} + H_2O + K^+ \rightarrow Wm_{II} + Ep + Ab + Grt_I$
- Step 3)
  $\text{K-feldspar} + Na+ \rightarrow Ab + K^+$

Image Analysis (Modal proportion analysis)

From BSE images composite scripts with open source ImageJ software (Rasband, 1997; Abramoff 2004) have been used to separate individual mineral phases and then obtain their amount. The automated scripts allow to separate object using their colours in the grey scale. BSE images are well suited for this purpose. This analysis has been performed on 4 main microdomain: Pl_I cores, allowing to quantify the amount of Ep, Wm_{II} and Ab constituting the fine-grained aggregates that substitute Pl_I; Pl_I rims, constituted by coarse grained Wm_{II} + Pl_I-facing Grt; Wm_I, constituted by Wm_{II} + Ep + Ab + Grt_I + Qtz; Bt_I, constituted by Bt_I + Wm_{II} + Bt_I-facing Grt. The automated scripts run 8-bit conversion, set thresholds to specific interval from 0 (black) to 255 (white), previously set on the basis of the grey intervals at BSE images for each phase (0-35 Ab and Qtz; 35-75 Wm; 76-125 Ep; 95-135 Bt; 145-255 Grt). The obtained images are now binary (black and white) where black corresponds to the

investigated phase; the last step is the measurement of the black pixels with respect to the total (Fig. 9, Tab. 2). The latter quantity corresponds to the amount of the investigated phase. The same procedure is repeated for each mineral phase (i.e. Ep, Ab, Wm, Grt). Table 2 reports the mean results of these calculations performed on Pl_I (cores and rims), Bt_I, Wm_I microdomains. The obtained values are combined with modal amounts of each phase to calculate the bulk compositions for each microdomain.

Figure 10. Qualitative chemical profiles along the Grt_I coronas at Bt_I – Pl_I boundaries.

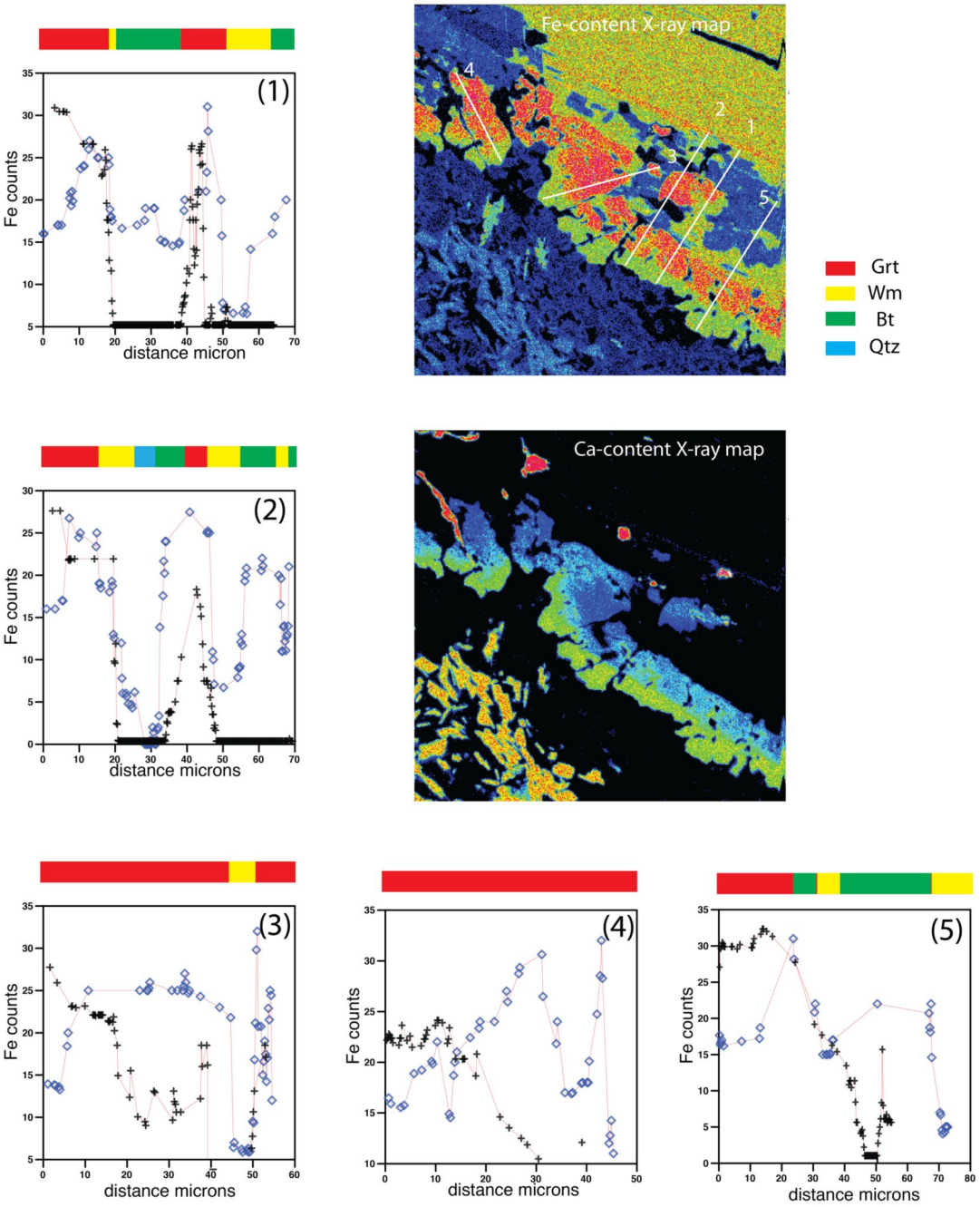

Fe-content X-ray map shows the location of the profile lines. On top of the chemical profiles different colors correspond to the crossed mineral phases.

Figure Table 2. A) Modal amounts obtained from the image analysis on BtI, WmI, WmII+Grt, PlI microdomains; B) Effective bulk compositions obtained by combining modal amounts from image analysis and mineral phases compositions of Table 1.

A) Modal amounts from analysis of SEM-BSE images

Domain-Sample	*Grt*	*Bt*	*Ep*	*Wm*	*Ab+Qtz*	*Bkg*	*SUM*
BtI							
260_a	5	41	0	15	3	35	99
261_a	6	28		36	5	27	102
262_a	6	22		29	4	40	101
MZ1AB_X5	7	32	13	29	18	0	99
141	18	40		25	21	0	104
260_a	8	64	0	23	5 removed		100
261_a	8	37	0	48	7 removed		100
262_a	10	36	0	48	7 removed		100
mean	***10***	***42***	***3***	***35***	***11***	***0***	***101***
WmI							
265	8	0	15	59	14	0	96
259	11	0	10	67	14	0	102
mean	***9.5***	***0***	***12.5***	***63***	***14***	***0***	***99***
PlI_rim							
260_a	8	0	5	31	8	51	103
260_b	7		0	27	7	57	98
MZ1AB_X5	11	0	0	89	0	0	100
260_a	*15*	*0*	*10*	*60*	*15* removed		100
260_b	*17*	*0*	*0*	*66*	*17* removed		100
mean	***14***	***0***	***3***	***71***	***11***	***0***	***100***
PlI_core							
MZ1AB_X1_b	0	0	14	21	15	53	103
MZ1AB_X1_c	0	0	14	33	28	33	108
262_A	1	0	19	37	24	28	109
MZ1AB_x5a	0	0	31	46	24	0	101
268_a	0	0	15	36	46	0	97
MZ1AB_X1_b	0	0	28	42	30 removed		100
MZ1AB_X1_c	0	0	19	44	37 removed		100
262_A	1	0	23	46	30 removed		100
mean	***0***	***0***	***23***	***43***	***33***	***0***	***100***

B) Effective bulk compositions for individual sub-systems

Phase	amount %	Na2O	MgO	Al2O3	SiO2	K2O	CaO	TiO2	FeO	Fe2O3
Grt	10	0	2.83	21.33	38.82	0	6.04	0.17	32.97	0
Bt	42	0	7.27	14.54	37.71	9.72	0	4.18	24.17	0
Ep	3	0	0	27.12	39.18	0	23.79	0	0	8.39
Wm	35	0	3.17	26.43	49.45	10.58	0	0.15	6.64	0
Ab	11	11.62	0	19.57	69.3	0.06	0.04	0	0	0
tot	101.25									

Microdomain_BtI — Bulk Composition - wt%

sum	Na2O	MgO	Al2O3	SiO2	K2O	CaO	TiO2	FeO	Fe2O3
99.24	1.32	4.43	20.50	46.00	7.74	1.39	1.82	15.76	0.27

Phase	amount %	Na2O	MgO	Al2O3	SiO2	K2O	CaO	TiO2	FeO	Fe2O3
Grt	9.5	0	0.83	21.36	38.71	0	16.75	0	0	0
Bt	0									
Ep	12.5	0	0	27.12	39.18	0	23.79	0	0	8.39
Wm	63	0	1.34	26.25	49.51	11.1	0	0	6.13	0
Ab	14	11.82	0	19.25	68.9	0.3	0.03	0	0	0
tot	99									

Microdomain_WmI — Bulk Composition - wt%

sum	Na2O	MgO	Al2O3	SiO2	K2O	CaO	TiO2	FeO	Fe2O3
93.16	1.65	0.92	24.65	49.41	7.04	4.57	0.00	3.86	1.05

Phase	amount %	Na2O	MgO	Al2O3	SiO2	K2O	CaO	TiO2	FeO	Fe2O3
Grt	14	0	0.7	21.53	39.22	0	17.62	0	22.49	0
Bt	0									
Ep	3	0	0	27.12	39.18	0	23.79	0	0	8.39
Wm	71	0	2.18	30.13	49.87	10.79	0	0.14	2.47	0
Ab	11	11.77	0	19.5	68.5	0.3	0.2	0	0	0
tot	100									

Microdomain_PlI rim — Bulk Composition - wt%

sum	Na2O	MgO	Al2O3	SiO2	K2O	CaO	TiO2	FeO	Fe2O3
96.15	1.27	1.06	24.86	49.74	7.97	3.34	0.00	7.64	0.27

Phase	amount %	Na2O	MgO	Al2O3	SiO2	K2O	CaO	TiO2	FeO	Fe2O3
Grt	0									
Bt	0									
Ep	23	0	0	27.12	39.18	0	23.79	0	0	8.39
Wm	43	0	2.68	28.8	53.7	5.61	0	0	4.71	0
Ab	33	11.84	0	19.72	69.47	0.12	0.27	0	0	0
tot	100									

Microdomain_PlI core — Bulk Composition - wt%

sum	Na2O	MgO	Al2O3	SiO2	K2O	CaO	TiO2	FeO	Fe2O3
97.55	3.95	1.15	25.19	55.25	2.44	5.62	0.00	2.01	1.95

Pressure-Temperature conditions

Pressure estimates have been performed using Si^{4+} content in phengitic micas (Wm_I and Wm_{II}) (Massonne and Schreyer 1987); temperature estimates have been done using Ti and Al^{VI} contents in biotite (Schreurs 1985; Henry *et al.*, 2005), garnet-biotite exchange (Thompson 1976; Holdaway and Lee 1977; Ferry and Spear 1978; Dasgupta *et al.* 1991; Perchuk 1991; Bhattacharaya *et al.* 1992), garnet-white mica (Green and Hellman, 1982; Hynes and Forest, 1988).

Bt_I microdomain

Temperatures of 700 to 730°C (Table 1) are estimated for highest Ti-rich biotite (Bt_I) using the calibration of Henry *et al.* (2005) with a standard deviation of 30°C. Such temperatures may be addressed to the pre-Alpine stage of this rock and likely to the igneous crystallization phase. At the rims of the Bt_I, Grt_I is in contact with biotite with different compositions from Bt_I, Fe-Ti-rich, to Bt_{II} Ti-poor Mg-richer; the garnet-biotite calibrations applied on these pairs give three *T* intervals: 400-550°C, 550-620°C and 650-750°C in a range of *P* = 3-10kbar. The lower *T* interval corresponds to Bt_{II} with a more re-equilibrated composition. At the same rims Wm_{II}+Grt_I also occurs and the application of garnet-phengite thermometer gives a *T* intervals 500°±50C in the pressure range 3-10kbar.

Pressure estimates using the Si^{4+} content in phengitic micas (Wm_{II}) give *P* = 10-12.5 kbar in the *T* range 450-600°C.

Pl microdomain

Pl_I microdomains are characterized by coarse rim of Wm_{II} + Grt_I. Garnet-phengite calibrations applied on these pairs give *T* = 370±30°C in the pressure range of

3-10kbar. Si^{4+} content in Wm_{II} gives *P* = 10-12.5 kbar in the *T* range 450-650°C.

Summing up, a pre-Alpine stage is still recorded by the Bt_I composition that suggest *T* = 700-730°C, while no pressure estimates are available for this stage. The Alpine re-equilibration occurred at *T* between 450 and 550°C and minimum *P* at 10-12 kbar.

Discussion

The coronitic metagranite of the *Lago della Vecchia* is characterized by the preservation of igneous textures but a partial to total replacement of primary minerals. The Alpine evolution produced reactions and corona textures by the exchange of chemical elements, occurring at different times, between adjacent minerals.

Igneous biotite is partly preserved, white mica and quartz grains record re-equilibration but relicts are still preserved; plagioclase and K-feldspar are nearly completely replaced by Alpine parageneses. The mineralogy, grain-size and thickness of the Alpine reaction rims and corona depend on the nature of the reacting domains, chemistry and position in the rock body of the reacting microdomains.

The microstructural study presented here show the development of a series of textures:

- Biotite microdomain at contact with plagioclase – two coronas are observed: 1) Bt_{II} + Wm_{II} + Alm-rich Grt_I; 2) Wm_{II} + Grs-rich Grt coronas;
- White mica microdomain with plagioclase: a single Wm_{II} + Grt + Ep + Ab corona develops;
- K-feldspar microdomain with plagioclase: a single Ab + Wm_{II} ± Ep ± Grt corona develops;
- Plagioclase core microdomain: Ab + Wm_{II} (fine-grained) + Ep ± Grt;
- K-feldspar core microdomain: large igneous grains are partly to completely replaced by Ab from the plagioclase-K-feldspar boundaries or along fractures.

These microstructures and chemical patterns display peculiar characters elsewhere described for similar rocks, with some differences.

From the Sesia-Lanzo Zone the example of the Mucrone and the Mars metagranites and metagranodiorites are well known (Oberhansli, 1985; Koons *et al.* 1987; Zucali *et al.*, 2002; Bruno and Rubbo, 2006). They are characterized by microstructural relicts of the igneous assemblages, now completely replaced by the eclogite facies Alpine mineral assemblages, except for local biotite and amphibole (Rubbo *et al.*, 1999; Zucali *et al.* 2002b).

Despite the microstructural similarities, the presented microstructures differ from those of the Monte Mucrone-Mars for the metamorphic assemblages produced within original igneous plagioclase microdomain and, in particular, the absence of jadeite in the rocks of the *Lago della Vecchia*. The plagioclase microdomain in the Mucrone metagranite is replaced by aggregates of Jd + Grt + Wm + Qtz while at the *Lago della Vecchia*, Zo + Wm + Grt + Qtz + Ab aggregates replace the plagioclase. Microstructures and mineral assemblages within the other igneous domains are similar as well the compositions. Moreover, similar garnet corona have been described for the eclogite facies Alpine metamorphism from metapelites of the Monte Rosa nappe, Western Italian Alps (Keller *et al.*, 2004; 2006). The microstructures and chemical variations are described as enhanced by mass transfer through short-circuit diffusion, where nanometer wide channels occur as direct links between reaction fronts, providing fast diffusion preferred paths. Chemical profiles of the garnet corona between Bt_I and Pl_I domains suggest diffusive mass transfer for the growth of garnet during the high pressure metamorphic event as inferred by Keller *et al.* (2006) and Bruno and Rubbo (2006).

The garnet growth may have started with an homogenous composition (Alm-rich), produced until Pl was stable; when Pl_I released Ca the Grs content consequently increased, starting from the grain boundary with Pl_I and Alm decreased (Fig. 10). Grs content increase stopped when Zo became stable. At this point the Ab should have become unstable as the reaction curve Ab = Jd + Qtz was crossed, but this does not seem to have occurred in this rocks. However, as suggested by Konrad-Schmolke (2005), the complex evolution of garnet growth and the limited element supply during the growth evolution may mask the thermobarometric history.

The calculated composition of the plagioclase core (Table 2; Plagioclase microdomain) differs from an igneous oligoclase composition (e.g. $Na_{0.8}Ca_{0.2}Al_{1.2}Si_{2.8}O_8$); the reconstructed Pl composition is enriched in K_2O (2.50 wt%), MgO (1.15 wt%), FeO (2.01 wt%), Fe_2O_3 (1.95 wt%) and H_2O (e.g. Zo and Wm) and it is depleted in Na_2O (< 4.00 wt%).

Following the combination of microstructural criteria and chemical observations it is possible to describe unbalanced qualitative reactions, involving the igneous mineral chemistry and adding other chemical species to account for diffusion, most likely enhanced by the H_2O produced by the progressive break-down of biotite at high pressure (Fig. 11):

- $Bt_I \rightarrow Bt_{II} + Wm_{II}$ + Alm-rich Grt_I
- $Bt_I + Ca^{2+}$ (Pl_I) $\rightarrow Bt_{II} + Wm_{II}$ + Grs-rich Grt_I
- $Wm_I + Ca^{2+}$ (Pl_I) $\rightarrow Wm_{II}$ + Grt
- $Pl_I + H_2O + K^+ + Ti^{4+} + Mg^{2+} + Fe^{2+} \rightarrow$ Ab + Wm_{II} + Ep ± Grt
- Pl_I rim + $H_2O + K^+ + Ti^{4+} + Mg^{2+} + Fe^{2+} \rightarrow Wm_{II}$ + Ab ± Ep ± Grt_I
- Pl_I core + $H_2O + K^+ \rightarrow Wm_{II}$ + Ep + Ab + Grt_I
- K-feldspar + Na+ → Ab + K^+

Thermobarometrical estimates of the Alpine evolution (Fig. 11) point to a blueschists facies conditions re-equilibration at P = 12.5kbar and T = 450-550°C, where the pressure are limited due to the absence of jadeite or omphacite in the assemblage.

Conversely, the mesoscopic observations (Figs. 2, 3) and the field continuity with the rest of the Eclogitic Micaschists Complex, where the stable associations developed under eclogite facies conditions at P > 20kbar and T = 500-550°C (Tropper and Essene, 2002; Zucali 2002a, b; Zucali and Spalla, 2011), suggest consideration of similar *P-T* conditions for these rocks.

In support of this hypothesis, garnet growth modelling for the Monte Mucrone (Bruno and Rubbo, 2006) predicts peak conditions of P > 16kbar and T = 550-600°C; qualitative comparison of chemical evolutions of the garnet corona from the *Lago della Vecchia* with those described for the Monte Mucrone and their similar size (30-70 µm) allows a similar growth model and, consequently, inference of similar *P-T* conditions of growth for the Grt_I corona, in agreement with mesoscopic observations (Fig. 2). But there is still a discrepancy regarding the absence of Na-pyroxene and the widespread presence of Ab within Pl and Kfs domains, since albite should be replaced by high pressure assemblages as jadeite + quartz, while attaining eclogite facies conditions.

Future analyses should aim at defining the *P-T* conditions reached by surrounding deformed metagranites to discriminate between the two possible interpretations: i) the coronitic metagranites only recorded part of the prograde path while the surrounding rocks recorded peak conditions (e.g. Arenas and Martinez Catalán, 2002); ii) the *Lago della Vecchia* metagranites suffered lower pressure conditions compared to the southern part of the same Eclogitic Micaschists Complex (e.g. Monte Mucrone-Monte Mars area).

The *P-T* estimates for the igneous stage provide T = 700-730°C, obtained from the igneous Bt_I compositions. No other constraints are available for this pre-Alpine stage.

Figure 11. *P-T*-t path of the *Lago della Vecchia* metagranite

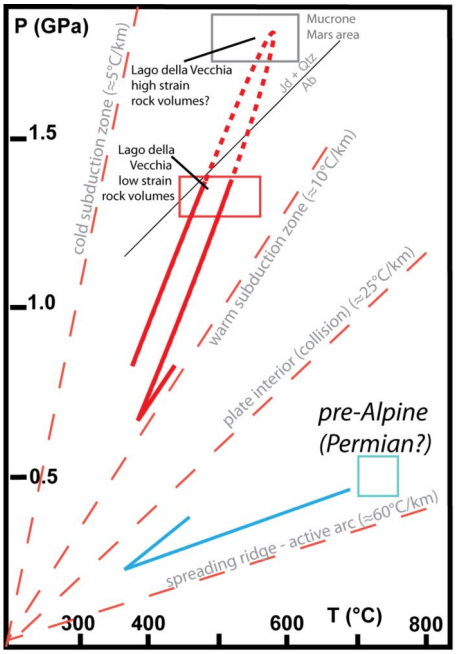

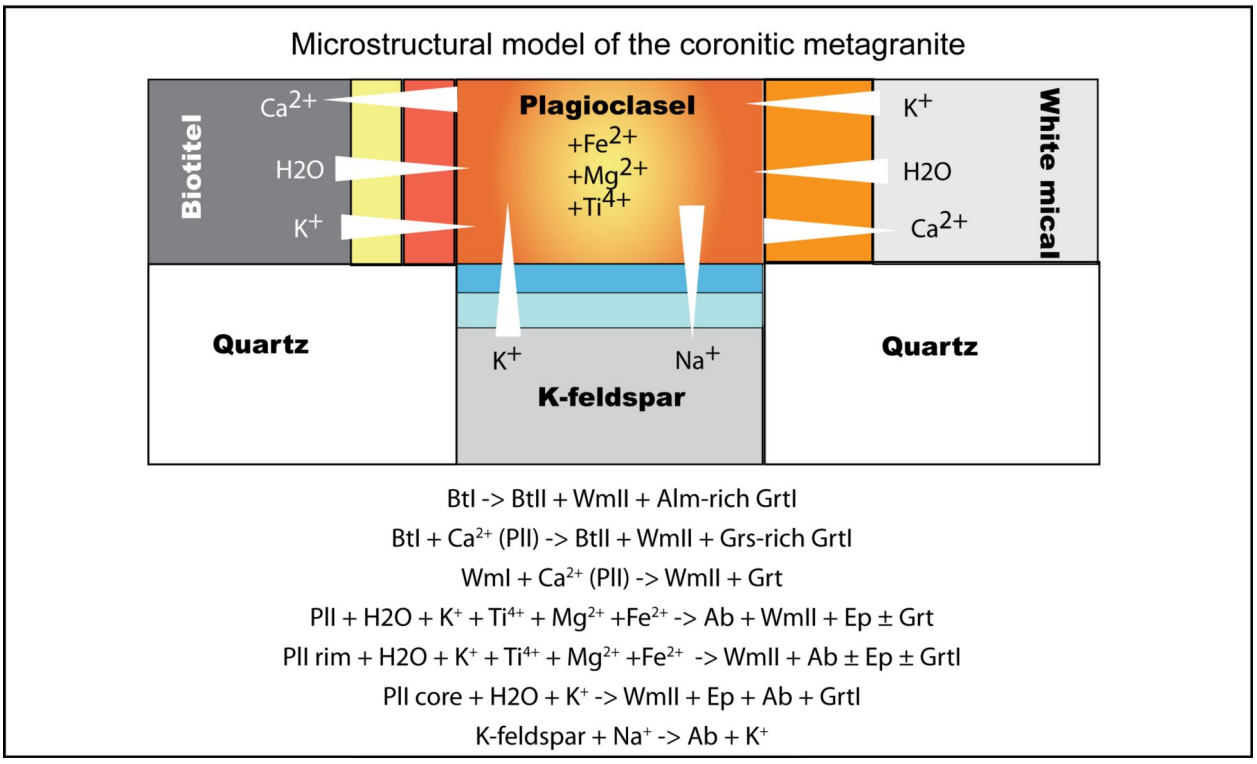

P-T-t path of the *Lago della Vecchia* metagranite using microstructural analysis and thermobarometrical estimates from this work and *P-T* estimates from Zucali *et al.* (2002a) for comparison with similar evolution of the high strain rock volumes within the same Eclogitic Micaschists Complex and reference to pre-Alpine igneous crystallization *P-T* conditions.

Conclusions

The absence of deformation in these samples of the *Lago della Vecchia* area permits the preservation of pre-eclogitic microstructures and assemblages, even where the Alpine metamorphic overprint is penetrative (i.e. the Eclogite Micaschists Complex).

The eclogite-facies re-equilibration is also testified by assemblages that resemble those of other area of the Eclogitic Micaschists Complex.

Coronitic microstructures reflect the stages of the prograde biotite break-down thorough a series of continuous reactions that progressively change the biotite composition, producing garnet coronas. Igneous primary plagioclase breakdown occurs during the burial stages and allows stabilization of Ca-phases as epidote and grossular-rich garnet coronas. Plagioclase break-down is also associated with the growth of hydrous minerals such as phengitic mica and epidote that imply a contribution of H_2O and K_2O to the reactions.

H_2O may have an important role on the diffusive mass transfer, enhancing metamorphic reactions and providing chemical feeds to all reactions observed in the coronitic metagranite of the *Lago della Vecchia*: e.g. plagioclaseI cores, plagioclaseI rims, biotiteI rims, white micaI rims.

Deformation is absent within the studied samples of coronitic metagranite of the *Lago della Vecchia* but it is evident that the transformations are much more evolved within deformed volumes of metagranite than in the undeformed ones as shown in other field-based studies (Spalla et al, 2004) or at laboratory scale (Holyhoke and Tullis, 2006). Within the *Lago della Vecchia* metagranite deformation enhanced reaction kinetics in the progress of metamorphic transformations, as previously suggested by Hobbs *et al.* (2010) although the role of fluids during pre-burial and burial stages is still not understood.

Acknowledgments

Gisella Rebay is friendly thanked for her support to various versions of this paper. Juan Gomez Barreiro and Gordon Lister are also greatly thanked for careful reviews.

References

Abramoff MD, Magelhaes PJ, Ram SJ (2004) Image Processing with ImageJ. Biophotonics International 11: 36-42.

Arenas R and Catalàn RM (2002) Prograde development of corona textures in metagabbros of the Sobrado unit (Ordenes Complex, northwestern Iberian Massif). Geological Society of America Special Publications. 364: 73-88.

Babist J, Handy MR, Konrad-Schmolke M, Hammerschmidt K (2006) Precollisional, multistage exhumation of subducted continental crust: The Sesia Zone, western Alps. Tectonics 25: 1-25.

Bhattacharaya A, Mohanty L, Maji A, Sen SK, Raith M (1992) Non-ideal mixing in the phlogopite-annite-binary:constraints from experimental data on Mg-Fe partitioning and a formulation of the biotite-garnet geothermometer. Contributions to Mineralogy and Petrology 11: 87-93.

Bigioggero B, Colombo A, Del Moro A, Gregnanin A, Macera P, et al. (1994) he Oligocene Valle Cervo Pluton: an example of shoshonitic magmatism in the Western Italian Alps. Mem Soc Geol It 46: 409-421.

Bruno, M., and Rubbo, M., 2006, The metamorphic history of Monte Mucrone metagranodiorite constrained by garnet growth modelling: Per. Mineral. v. 75, p, 3--22.

Compagnoni R (1977) The Sesia-Lanzo zone: high-pressure low-temperature metamorphism in the Austroalpine continental margin. Rendiconti della Società Italiana di Mineralogia e Petrologia Rendiconti della Società Italiana di Mineralogia e Petrologia 33: 335-374.

Compagnoni R, Dal Piaz GV, Hunziker JC, Gosso G, Lombardo B, et al. (1977) The Sesia-Lanzo Zone: a slice of continental crust, with alpine HP-LT assemblages in the Western Italian Alps. Rendiconti della Società Italiana di Mineralogia e Petrologia 33: 281-334.

Dal Piaz GV, Cortina G, Del Moro A, Martin S, Pennacchioni G, et al. (2001) Tertiary age and paleostructural inferences of the eclogitic imprint in the Austroalpine outliers and Zermatt-Saas ophiolite, western Alps. International Journal of Earth Sciences 90: 66-684.

Dasgupta S, Sengupta P, Guha D, Fukuoka M (1991) A refined garnet-biotite Fe-Mg exchange geothermometer and its application in amphibolites and granulites. Contributions to Mineralogy and Petrology 109: 130-137.

Deer WA, Howie RA, Zussman J (1996) An Introduction to the Rock-Forming Minerals. Prentice Hall. 712 p.

Desmons J, O'Neil R (1978) Oxigen and Hydrogen isotope composition of eclogites and associated rocks from the Eastern Sesia Zone (Western Alps, Italy). Contributions to Mineralogy and Petrology: 79-85.

Duchene S, Blichert TJ, Luais B, Telouk P, Lardeaux JM, et al. (1997) The Lu-Hf dating of garnets and the ages of the Alpine high-pressure metamorphism. Nature (London) 387: 586-589.

Ferry JM, Spear FS (1978) Experimental calibration of the partitioning of Fe and Mg between biotite and garnet. Contrib Mineral Petrol Contributions to Mineralogy and Petrology 66: 113-117.

Green TH, Hellman PL (1982) Fe-Mg partitioning between coexisting garnet and phengite at high pressure, and comments on a garnet-phengite geothermometer. Lithos 15: 253-266.

Handy MR, Babist J, Wagner C, Rosemberg C, Konrad M (2005) Decoupling and its relation to strain partitioning in continental lithosphere: insight from the Periadriatic fault system (European Alps). In: Gapais D, Brun JP, Cobbold P, editors. Deformation Mechanisms, Rheology and Tectonics: from Minerals to the Lithosphere. Geological Society, London, Special Pubblications. pp. 249-276.

Henry, B., Guidotti, C.V., and Thomson, J.A., 2005, The Ti-saturation surface for low-to-medium pressure metapelitic biotite: Implications for Geothermometry and Ti-substitution Mechanisms.: American Mineralogist v. 90, p, 316--328.

Hobbs, B.E., Ord, A., Spalla, M.I., Gosso, G., and Zucali, M., 2010, The interaction of deformation and metamorphic reactions: Geological Society of London Special Publication. In: Advances in interpretation of geological processes: refinement of multi-scale data and integration in numerical modelling v. 332, p, 189--222.

Holdaway MJ, Lee SM (1977) Fe-Mg cordierite stability in high-grade pelitic rocks based on experimental, theoretical and natural observations. Contrib Miner Petrol Contributions to Mineralogy and Petrology 63: 175-198.

Holyoke III, C.W., and Tullis, J., 2006, The interaction between reaction and deformation: an experimental study using a biotite+ plagioclase+ quartz gneiss: Journal of Metamorphic Geology v. 24, p, 743--762.

Hynes A, Forest RC (1988) Empirical garnet-muscovite geothermometry in low-grade metapelites, Selwyn Range (Canadian Rockies). Journ metam Geol Journal of metamorphic Geology 6: 297-309.

Inger S, Ramsbotham W, Cliff RA, Rex DC (1996) Metamorphic evolution of the Sesia-Lanzo Zone, Western Alps: time constraints from multi-system geochronology. Contribution to Mineralogy and Petrology 126: 152-168.

Kapferer, N., Mercolli, I., and Berger, A., 2011, The composition and evolution of an Oligocene regolith on top of the Sesia–Lanzo Zone (Western Alps): International Journal of Earth Sciences v. 1--13.

Keller, L.M., Abart, R., Stünitz, H., and De Capitani, C., 2004, Deformation, mass transfer and mineral reactions in an eclogite facies shear zone in a polymetamorphic metapelite (Monte Rosa nappe, western Alps): Journal of Metamorphic Geology v. 22, p, 97--118.

Keller, L.M., Abart, R., Wirth, R., Schmid, D.W., and Kunze, K., 2006, Enhanced mass transfer through short-circuit diffusion: Growth of garnet reaction rims at eclogite facies conditions: American Mineralogist v. 91, p, 1024.

Kohn, M.J., 2003, Geochemical zoning in metamorphic minerals: The crust. Treatise on Geochemistry v. 3, p, 229--261.

Konrad-Schmolke, M., Handy, M.R., Babist, J., and O'Brien, P.J., 2005, Thermodynamic modelling of diffusion-controlled garnet growth: Contributions to Mineralogy and Petrology v. 149, p, 181--195.

Konrad-Schmolke M, Babist J, Handy MR, O'Brien JK (2006) The Physico-Chemical Properties of a Subducted Slab from Garnet Zonation Patterns (Sesia Zone, Western Alps). Journal of Petrology 2123-2148.

Koons PO (1986) Relative geobarometry from high-pressure rocks of quartzofeldspathic composition from the Sesia Zone, Western Alps, Italy. Contribution to Mineralogy and Petrology 93: 322-334.

Koons PO, Rubie DC, Frueh-Green G (1987) The effects of disequilibrium and deformation on the mineralogical evolution of quartz-diorite during metamorphism in the eclogite facies. Journ Petrol Journal of Petrology 28: 679-700.

Kretz, R., 1983, Symbols for rock-forming minerals: American Mineralogist v. 68, p, 277--279.

Lardeaux JM, Spalla MI (1991) From granulites to eclogites in the Sesia zone (Italian Western Alps): a record of the opening and closure of the Piedmont ocean. Journal of Metamamorphic Geology 9: 35-59.

Massonne HJ, Schreyer W (1987) Phengite geobarometry based on the limiting assemblage with k-feldspar, phlogopite and quartz. Contributions to Mineralogy and Petrology 96: 212-224.

Matsumoto K, Hirajima T (2004) Prograde lawsonite from the southern eclogitic micaschist complex in the Sesia Zone, Western Alps, Italy. Italia 2004; 32nd international geological congress; abstracts.: 107.

Oberhänsli R, Hunziker JC, Martinotti G, Stern WB (1985) Geochemistry, gheochronology and Petrology of Monte Mucrone: an example of Eo-Alpine eclogitisation of Permian granitoids in the Sesia-Lanzo Zone, Western Alps, Italy. Chemical Geology 52: 165-184.

Paquette JL, Chopin C, Pecaut JJ (1989) U-Pb zircon, Rb-Sr and Sm-Nd geochronology of high- to very-highpressure meta-acidic rocks from the Western Alps. Contribution to Mineralogy and Petrology 101: 280-289.

Passchier CW, Urai JL, van Loon J, Williams PF (1981) Structural geology of the central Sesia Lanzo Zone. Geologie en Mijnbouw 60: 497-507;.

Perchuk LL (1991) Progress in metamorphic and magmatic petrology; a memorial volume in honor of D. S. Korzhinskiy. Univ. Press. Cambridge, United Kingdom. 1991.

Pognante U (1989a) Lawsonite, blueschist and eclogite formation in the southern Sesia Zone (Western Alps, Italy). European Journal of Mineralogy European Journal of Mineralogy 1: 89-104.

Pognante U (1989b) Tectonic implications of lawsonite formation in the Sesia zone (Western Alps). Tectonophysics 162: 219-227.

Polino R, Dal Piaz GV, Gosso G (1990) Tectonic erosion at the Adria margin and accretionary processes for the Cretaceous orogeny of the Alps. In: Roure F, Heitzmann P, Polino R, editors. Deep structure of the Alps. pp. 345-367.

Prenzel, J., Abart, R., and Keller, L., 2009, Complex chemical zoning in eclogite facies garnet reaction rims: the role of grain boundary diffusion: Mineralogy and Petrology v. 95, p, 303--313.

Rasband WS (1997) ImageJ. National Institutes of Health, Bethesda, Maryland, USA, http://rsb.info.nih.gov/ij/

Rebay G, Spalla MI (2001) Emplacement at granulite facies conditions of the Sesia–Lanzo metagabbros: an early record of Permian rifting? Lithos 58: 85-104.

Romer RL, Schärer U, Steck A (1996) Alpine and pre-Alpine magmatism in the root zone of the Western Alps. Contribution to Mineralogy and Petrology 123: 138-158.

Rubatto D, Gebauer D, Compagnoni R (1999) Dating of eclogite-facies zircons; the age of Alpine metamorphism in the Sesia-Lanzo Zone (Western Alps). Earth and Planetary Science Letters 167: 141-158.

Rubbo M, Borghi A, Compagnoni R (1999) Thermodynamic analysis of garnet growth zoning in eclogite facies granodiorite from M. Mucrone, Sesia Zone, western Italian Alps. Contributions to Mineralogy and Petrology 137: 289-303.

Ruffet G, Gruau G, Ballevre M, Feraud G, Philippot P (1997) Rb-Sr and (super 40) Ar- (super 39) Ar laser probe dating of high-pressure phengites from the Sesia Zone (Western Alps); underscoring of excess argon and new age constraints on the high-pressure metamorphism. Chemical Geology 141: 1-18.

Scheuring B, Ahrendt H, Hunziker JC, Zingg A (1973) Paleobotanical and geochronological evidence for the Alpine age of the metamorphism in the Sesia-Zone. Geologische Rundschau Geologische Rundschau 63: 305-326.

Schreurs J (1985) Prograde metamorphism of metapelites, garnet-biotite thermometry and prograde chenges of biotite chemistry in high grade rocks of West Uusimaa, southwest Finland. Lithos Lithos 18: 69-80.

Spalla MI, Zulbati F (2004) Structural and petrographic map of the southern Sesia-Lanzo Zone; Monte Soglio-Rocca Canavese, Western Alps, Italy. Memorie di Scienze Geologiche 55: 119-127 ; 1 sheet.

Spalla, M.I., Zucali, M., Salvi, F., Gosso, G., and Gazzola, D., 2004, Tectono-metamorphic map of the Languard-Campo; Serie del Tonale nappes between upper Val Camonica and Valtellina; Central Italian Alps, Austroalpine domain: Memorie di Scienze Geologiche v. 55, p, 105--118 ; 1 sheet, 1 CD-ROM.

Thompson AB (1976) Mineral reactions in pelitic rocks, I. Predictions of P-T-X (Fe-Mg) phase realtions. II Calculation of some P-T-X (Fe-Mg) phase relations. American Journal of Sciences 276: 201-254.

Tropper P, Essene EJ, Sharp ZD, Hunziker JC (1999) Application of K-feldspar-jadeite-quartz barometry to eclogite facies metagranites and metapelites in the Sesia Lanzo Zone (Western Alps, Italy. Journal of Metamorphic Geology 17: 195-209.

Vernon, R.H., and Clarke, G.L., 2008, Principles of metamorphic petrology: Cambridge University Press, 446 p.

Zanoni D, Bado L, Spalla MI, Zucali M, Gosso G (2008) Structural analysis of the northeastern margin of the Tertiary intrusive stock of Biella (Western Alps, Italy). Bollettino della Societa Geologica Italiana 127: 125-140.

Zucali M (2002a) Foliation map of the “Eclogitic Micaschists Complex” (Monte Mucrone – Monte Mars – Mombarone, Sesia-Lanzo Zone, Italy). Mem Sc Geol 54: 86-100.

Zucali M, Spalla MI, Gosso G (2002b) Strain Partitioning And Fabric Evolution As A Correlation Tool: The Example Of The Eclogitic Micaschists Complex In The Sesia-Lanzo Zone (Monte Mucrone – Monte Mars, Western Alps Italy). Schweizerische Mineralogische und Petrographische Mitteilungen 82: 429-454.

Zucali M, Spalla MI, Gosso G, Racchetti S, Zulbati F (2004) Prograde LWS-KY Transition During Subduction Of The Alpine Continental Crust Of The Sesia-Lanzo Zone: The Ivozio Complex. In: Evolution of the western Alps: insights from metamorphism, structural geology, tectonics and geochronology Journal of Virtual Explorer. V. 16.

Zucali and Spalla (2011) – Prograde Lawsonite During The Flow Of Continental Crust In The Alpine Subduction: Strain Vs. Metamorphism Partitioning, A Field-Analysis Approach To Infer Tectonometamorphic Evolutions (Sesia-Lanzo Zone, Western Italian Alps).: Journal of Structural Geology v. 33, p, 381--398.